Acta Geotechnica (2023) 18:235–263
https://doi.org/10.1007/s11440-022-01529-1

RESEARCH PAPER

Bounding surface plasticity model with reversal surfaces for the monotonic and cyclic shearing of sands

Taxiarchoula G. Limnaiou[1] · Achilleas G. Papadimitriou[1]

Received: 4 September 2021 / Accepted: 2 March 2022 / Published online: 22 April 2022
© The Author(s), under exclusive licence to Springer-Verlag GmbH Germany, part of Springer Nature 2022

Abstract
The paper describes the formulation and simulative potential of a constitutive model for monotonic and cyclic shearing of sands. It is a SANISAND-type model that does not consider a (small) yield surface and employs the last stress reversal point for defining both the elastic and the plastic strain rates. Emphasis is put on the updating of the stress reversal point to avoid stress-strain overshooting. It incorporates a fabric evolution index that scales the plastic modulus targeting strain accumulation with cycles and a post-liquefaction formulation affecting the dilatancy function. The paper includes the calibration process of the 14 model parameters. Model performance is verified against a large database of monotonic and cyclic shearing tests on Toyoura and Ottawa-F65 sands. To complement sand-specific data, empirical relations are used for validating the shear modulus at small strains, its degradation with cyclic shear strain, the corresponding increase in hysteretic damping, the evolving rates of volumetric and shear strain accumulation with cycles and the effect of relative density and stress level on liquefaction resistance. Model verification shows that a single set of sand-specific parameters may be used for both monotonic and cyclic shearing of any strain level, irrespective of stress level and relative density.

Keywords Bounding surface plasticity · Constitutive modeling · Cyclic loading · Liquefaction · Monotonic loading · Sands

1 Introduction

Accurate numerical analyses of boundary value problems of geotechnical structures rely on the use of properly calibrated constitutive models that are appropriate for the geomaterial and the loading at hand. For coarse-grained geomaterials like sands, users often employ different constitutive models and/or different calibrations of the same model, depending on the target loading (e.g., monotonic versus cyclic, cyclic due to earthquakes versus cyclic due to wave action). Given its complexity, the issue of cyclic loading of sands has attracted a lot of attention in the literature, leading to multiple publications of constitutive models. Some of them incorporate the well-established mechanical framework of Critical State Soil Mechanics ([50]), while others are based on hypoplasticity theory (e.g., [5, 25, 41]). Nowadays, a large percentage of the pertinent Critical State models is of the SANISAND–type, i.e., bounding surface models ([11, 13]) in which the peak and the dilatancy deviatoric stress ratios depend on the state parameter ψ ([6]). Although the term SANISAND was coined in 2008 by Taiebat and Dafalias [56], the concept was first proposed by Manzari and Dafalias [34] in their two-surface model and adopted thereafter by many. The reason for its popularity is that it enables successful simulations for any relative density or stress level with the same set of model parameters.

In many cases, the papers that present models for cyclic loading of sands include accurate simulations of monotonic response, as well as of few cyclic loading tests leading to liquefaction. Such a presentation, although possibly sufficient for monotonic loading, may not be adequately complete for cyclic loading, whose characteristics are highly dependent on cyclic shear strain level ([66]). As such, a complete model verification for cyclic loading should focus

✉ Taxiarchoula G. Limnaiou
tlimnaiou@gmail.com

Achilleas G. Papadimitriou
apapad@civil.ntua.gr

[1] School of Civil Engineering, National Technical University of Athens, Athens, Greece

distinctly on: a) small-strain response ("*elastic*" stiffness modulus and initial damping ratio), b) medium-strain response (shear modulus degradation and hysteretic damping ratio increase with cyclic strain amplitude; strain accumulation with number of cycles), c) large-strain response, mainly with emphasis on liquefaction resistance curves and post-liquefaction strain accumulation. The importance of these distinct cyclic shear strain regimes for proper simulations has started to attract attention in the literature lately. For example, McAllister et al. [37] showed that if "*elastic*" modulus stiffness of SANISAND models is calibrated on the basis of monotonic tests, it underestimates significantly the in situ shear wave velocity leading to erroneous prediction of seismic ground response. Similarly, specialized models are being formulated for proper simulation of strain accumulation with large number of (medium-strain) cycles (e.g., [27, 30]), an issue rarely studied in papers presenting cyclic models in the past. Finally, a multitude of recent papers deal specifically with post-liquefaction strain accumulation (e.g., [58, 74]), underlining its importance for accurate simulations of displacements of geostructures in a liquefaction regime. To the authors' knowledge, there are few papers that present model verifications for all 3 distinct cyclic shear strain regimes (e.g., [1, 8, 10, 42]). Of course, this does not mean that sophisticated cyclic models that are not verified in this manner are inaccurate. It only means that their users should be cautious when using them outside their verified cyclic shear strain range.

Concurrently, some of the models that have exhibited a satisfactory performance for cyclic loading may not be as accurate when it comes to monotonic loading (e.g., the NTUA-SAND model ([1]) requires a change in the values of 2 model parameters in order to capture the monotonic response). In addition, some promising cyclic models were never implemented in numerical codes (e.g., [42]), while models that have been implemented in such codes have not been necessarily verified for the whole range of cyclic loading response (e.g., [77]). It goes without saying that targeted verification may also come from use in boundary value problems (e.g., [76]), which may even be preferable from mere comparison with element test data (e.g., [35]). In this respect, one should acknowledge models that have been widely used throughout the years, at least for liquefaction-related problems (e.g., [12]). Such models should be considered as equally accurate, at least for the problems that they have been repeatedly used in the past.

Based on the above, there is a need for a constitutive model for sands, which will be able to capture accurately both the monotonic response (until the critical state) and the cyclic response (for any shear strain level) with a single set of parameters for any relative density and stress level. This is the goal of the SANISAND-type model presented herein, which also incorporates stress reversal surfaces ([38, 68]) facilitating the simulation of cyclic loading without a (small) yield surface. In this respect, it is a SANISAND-R model, a term introduced recently by Papadimitriou et al. [44]. It builds on the NTUA-SAND model ([1]), from which it inherits concepts like the small- and medium-strain nonlinearity and the fabric evolution index for large strain response, albeit modified. Stress reversals are appropriately updated in order to avoid the stress–strain overshooting problem ([14]), but also to establish that strain accumulation does not appear at very small-strain cyclic loading in accordance to the literature ([66]). Post-liquefaction strains are in focus with an appropriate modification of the dilatancy function. It should be clarified in advance that the proposed is, by-design, a general-purpose constitutive model for sands. This means that its accuracy may not always be equal to that of dedicated models. For example, the accuracy of a fabric-based anisotropic model (e.g., [44]) may be superior for monotonic loading; however, such a model can only be used successfully for boundary value problems related to static loading (e.g., [9, 45]). On the contrary, the proposed model provides the user with a satisfactory performance without a need for recalibration regardless of whether the problem is static, cyclic or dynamic. In the sequel, this paper presents the model formulation in Sect. 2, which is followed by the thorough calibration of its 14 model parameters in Sect. 3. Then, Sect. 4 presents an elaborate verification against monotonic and cyclic test data, while the paper ends in Sect. 5 with notes regarding the applicability of the proposed model and its limitations.

2 Model formulation

2.1 Constitutive model platform

The formulation of the model is presented in the multiaxial stress space and the equations are given in tensorial form. Second-order tensors are written in bold characters, so as to be distinguished from scalars, while normal stress components are considered effective. A superposed dot over scalar or tensorial quantities implies material time derivative or rate. A symbol **:** between 2 tensors denotes their double inner product or equivalently the trace (tr) of their product. Specifically, the strain tensor is depicted as $\boldsymbol{\varepsilon}$ and can be decomposed into its (scalar) volumetric component $\varepsilon_{vol} = \mathrm{tr}\boldsymbol{\varepsilon}$ and the (tensorial) deviatoric component $\boldsymbol{e} = \boldsymbol{\varepsilon} - (\varepsilon_{vol}/3)\,\boldsymbol{I}$, with $\boldsymbol{I}$ standing for the second-order identity tensor. Superscripts e and p denote the elastic and plastic part of strains, respectively. The effective stress tensor is symbolized by $\boldsymbol{\sigma}$ and consists of its hydrostatic component $p = (1/3)\mathrm{tr}\boldsymbol{\sigma}$ (i.e., the mean effective stress) and its

deviatoric component $\boldsymbol{s} = \boldsymbol{\sigma}–p\boldsymbol{I}$. Of great importance is also the deviatoric stress ratio tensor $\boldsymbol{r} = \boldsymbol{s}/p$, which is instrumental in the constitutive equations of this model. Given the above definitions, the basic model equations are founded on elasto-plasticity theory and are summarized, for brevity, in Table 1.

Note that, in Eq. (4), the inclusion of scalar-valued loading index Λ is Macauley-bracketed implying that the plastic strain rate is zero when $\Lambda < 0$ (unloading) or $\Lambda = 0$ (neutral loading), and nonzero in cases of loading ($\Lambda > 0$). In Eq. (5), the plastic strain rate direction is defined, with unit-norm tensor $\boldsymbol{n}$ constituting its deviatoric part. The $\boldsymbol{n}$ adopts all the properties of unit-norm tensors (i.e., $\boldsymbol{n} = \boldsymbol{n}^{\mathrm{T}}$, $\mathrm{tr}\boldsymbol{n} = 0$ and $\boldsymbol{n}\colon\boldsymbol{n} = 1$) and is determined according to the adopted mapping rule of the model. According to Eq. (6), loading takes place either with a combination of $\boldsymbol{n} : \dot{\boldsymbol{r}} > 0$ (p is always nonnegative) and $K_{\mathrm{p}} > 0$ (hardening response) or $\boldsymbol{n} : \dot{\boldsymbol{r}} < 0$ and $K_{\mathrm{p}} < 0$ (softening response). Considering all the above, a nonzero deviatoric stress ratio rate serves as the necessary condition for nonzero plastic strain rates. This concept, while quite realistic during shearing, should be used with caution in problems where loading under constant stress ratio prevails (e.g., one-dimensional consolidation). Note also that a nonzero deviatoric stress ratio rate is not a sufficient condition for nonzero plastic strain rates. This is because the so-called neutral loading ($\Lambda = 0$) may appear for tangential loading paths, where both $\boldsymbol{n} \neq 0$ and $\dot{\boldsymbol{r}} \neq 0$ continuously, but $\boldsymbol{n} : \dot{\boldsymbol{r}} = 0$ throughout the loading. In this sense, the model does not have a truly zero elastic range in stress space, as was clarified for such models in Dafalias and Taiebat [14].

2.2 Critical state behavior

The proposed model formulation incorporates the Critical State Theory of Soil Mechanics ([50]) by adopting a unique Critical State Surface (CSS) in the effective stress $\boldsymbol{\sigma}$ – void ratio e space. For its projection on the mean effective p – void ratio e space, i.e., for the Critical State Line (CSL), a power relation is adopted. Hence, for a given mean effective stress p, the corresponding critical value of void ratio e_{cs} on the CSL is given by ([12, 28]):

$$e_{\mathrm{cs}} = e_{\mathrm{ref}} - \lambda\left(\frac{p}{p_{\mathrm{atm}}}\right)^{\xi} \tag{10}$$

where e_{ref} is the reference value of void ratio at $p = 0$ controlling the position of CSL (a model parameter), p_{atm} is the atmospheric pressure (e.g., $p_{\mathrm{atm}} = 101.3$ kPa), and λ and ξ are nonnegative model parameters forming CSL's curvature and shape in the $(p – e)$ space.

The current state of the material is always identified with reference to the CSL through the state parameter ψ, which quantifies the difference between the current void ratio e and the corresponding critical state value e_{cs} at the current mean effective stress p via ([6]):

$$\psi = e - e_{\mathrm{cs}} \tag{11}$$

Parameter ψ determines the state of the material as a combined function of its density (through void ratio e) and its effective mean stress (through e_{cs}), expressing how far from critical is the current state. It is obvious that a state (e, p) above the CSL in the $(p – e)$ space corresponds to $\psi > 0$ and consequently to contractive behavior, while, on the contrary, a state below the CSL in the $(p – e)$ space

Table 1 Basic constitutive formulation

Description of equation	Constitutive equation	Eq. number	Notes/References
Volumetric component of strain rate	$\dot{\varepsilon}_{\mathrm{vol}} = \dot{\varepsilon}^{\mathrm{e}}_{\mathrm{vol}} + \dot{\varepsilon}^{\mathrm{p}}_{\mathrm{vol}}$	(1)	
Deviatoric component of strain rate	$\dot{\boldsymbol{e}}=\dot{\boldsymbol{e}}^{\mathrm{e}}+\dot{\boldsymbol{e}}^{\mathrm{p}}$	(2)	
Elastic strain rate per effective stress rate $\dot{\boldsymbol{\sigma}}$	$\dot{\boldsymbol{\varepsilon}}^{\mathrm{e}} = \dot{\boldsymbol{e}}^{\mathrm{e}} + \frac{\dot{\varepsilon}^{\mathrm{e}}_{\mathrm{vol}}}{3}\boldsymbol{I} = \frac{1}{2G_{\mathrm{t}}}\dot{\boldsymbol{s}} + \frac{\dot{p}}{3K_{\mathrm{t}}}\boldsymbol{I}$	(3)	G_{t} and K_{t}: tangential values of elastic shear and bulk moduli (Eqs. 21 & 23)
Plastic strain rate	$\dot{\boldsymbol{\varepsilon}}^{\mathrm{p}} = \dot{\boldsymbol{e}}^{\mathrm{p}} + \frac{\dot{\varepsilon}^{\mathrm{p}}_{\mathrm{vol}}}{3}\boldsymbol{I} = \langle\Lambda\rangle\boldsymbol{R}$	(4)	
Plastic strain rate direction	$\boldsymbol{R} = \boldsymbol{n} + (D/3)\boldsymbol{I}$	(5)	D: the dilatancy function (Eqs. 36 & 38)
Loading index per effective stress rate $\dot{\boldsymbol{\sigma}}$	$\Lambda = \frac{1}{K_{\mathrm{p}}}\boldsymbol{L} : \dot{\boldsymbol{\sigma}} = \frac{1}{K_{\mathrm{p}}}\boldsymbol{n} : p\dot{\boldsymbol{r}}$	(6)	K_{p}: the plastic modulus (Eq. 24)
Loading direction	$\boldsymbol{L} = \boldsymbol{n} - \frac{\boldsymbol{n}:\boldsymbol{r}}{3}\boldsymbol{I}$	(7)	
Effective stress rate per strain rate $\dot{\boldsymbol{\varepsilon}}$	$\dot{\boldsymbol{\sigma}} = 2G_{\mathrm{t}}\dot{\boldsymbol{e}} + K_{\mathrm{t}}\dot{\varepsilon}_{\mathrm{vol}}\boldsymbol{I} - \langle\Lambda\rangle(2G_{\mathrm{t}}\boldsymbol{n} + K_{\mathrm{t}}D\boldsymbol{I})$	(8)	
Loading index per strain rate $\dot{\boldsymbol{\varepsilon}}$	$\Lambda = \dfrac{2G_{\mathrm{t}}\boldsymbol{n} : \dot{\boldsymbol{e}} - (\boldsymbol{n} : \boldsymbol{r})K_{\mathrm{t}}\dot{\varepsilon}_{\mathrm{vol}}}{K_{\mathrm{p}} + 2G_{\mathrm{t}} - (\boldsymbol{n} : \boldsymbol{r})K_{\mathrm{t}}D}$	(9)	

corresponds to $\psi < 0$ and consequently to dilative behavior. The explicit incorporation of ψ in model equations, starting from the model surfaces in the next paragraph, is what gives the SANISAND character to this model.

2.3 Model surfaces

Being of the SANISAND-type, the proposed bounding surface model is stress ratio-driven. For the common case of loading in triaxial compression (TC), the critical state $M_{\mathrm{c}}^{\mathrm{c}}$, the bounding (or peak) $M_{\mathrm{c}}^{\mathrm{b}}$ and the dilatancy $M_{\mathrm{c}}^{\mathrm{d}}$ stress ratios (collectively $M_{\mathrm{c}}^{\mathrm{c,b,d}}$) are related to each other via the state parameter ψ, as follows:

$$M_{\mathrm{c}}^{\mathrm{b}} = M_{\mathrm{c}}^{\mathrm{c}} \exp\left(n^{\mathrm{b}}\langle -\psi \rangle\right) \tag{12}$$

$$M_{\mathrm{c}}^{\mathrm{d}} = M_{\mathrm{c}}^{\mathrm{c}} \exp\left(n^{\mathrm{d}}\psi\right) \tag{13}$$

where $M_{\mathrm{c}}^{\mathrm{c}}$, n^{b} and n^{d} are nonnegative model parameters. Note that the subscript c depicts that loading is in triaxial compression, while superscripts c, b or d clarify which of the three stress ratios is of interest. These exponential equations are adopted from Li and Dafalias [26] and Dafalias and Manzari [12]. Note also that here Macauley brackets appear in Eq. (12) to make it qualitatively compatible with the linear form of this equation in Manzari and Dafalias [34]. Hence, based on Eqs. (12) and (13), for dilative states where $\psi < 0$, $M_{\mathrm{c}}^{\mathrm{d}} < M_{\mathrm{c}}^{\mathrm{c}} < M_{\mathrm{c}}^{\mathrm{b}}$ holds. This implies that the peak stress ratio is higher than the critical state ratio, while the dilatancy stress ratio is lower than both of them. Similarly, for contractive states ($\psi > 0$) $M_{\mathrm{c}}^{\mathrm{d}} > M_{\mathrm{c}}^{\mathrm{c}} = M_{\mathrm{c}}^{\mathrm{b}}$ holds, implying purely contractive response (since the $M_{\mathrm{c}}^{\mathrm{d}}$ is not reached) and attainment of the peak stress ratio at critical state.

The generalization of these three stress ratios in multiaxial stress space takes the form of surfaces, namely the critical state, the bounding and the dilatancy surface. All three surfaces have the shape of an open cone, with their apex on the origin of stress space, are homologous, and their apertures are defined by the stress ratio values M_{θ}^{c}, M_{θ}^{b} and M_{θ}^{d}, respectively. The subscript θ in the foregoing stress ratio values depicts that this generalization is performed with the aid of the Lode angle θ, that is hereby defined in terms of the unit-deviatoric loading direction tensor $\boldsymbol{n}$, according to:

$$\cos(3\theta) = \sqrt{6}tr\left(\boldsymbol{n}^3\right) = 3\sqrt{6}\,\det \boldsymbol{n} \tag{14}$$

where det is the determinant of a (second-order) tensor. Based on its definition, angle θ ranges between 0° and 60°, where 0° corresponds to loading in triaxial compression (TC) and 60° to triaxial extension (TE). All the intermediate values of θ correspond to non-triaxial loading conditions. Hence, the M stress ratio of the aforementioned surfaces can be defined as a continuous function of angle θ. In this model, this function is depicted by g and is used as follows:

$$M_{\theta}^{\mathrm{c,b,d}} = g(\theta, c)\, M_{\mathrm{c}}^{\mathrm{c,b,d}} \tag{15}$$

where $c = M_{\mathrm{e}}^{\mathrm{c}}/M_{\mathrm{c}}^{\mathrm{c}}$ is a nonnegative model parameter that is equal to the ratio of the critical stress ratio in triaxial extension (TE) over that in TC. In this paper, the adopted $g(\theta,c)$ function is borrowed from Loukidis and Salgado [33], although its more general form (involving 3 independent parameters) dates back to van Eekelen [18]. It reads:

$$g(\theta, c) = \frac{2^{\mu} c}{\left[1 + c^{1/\mu} - (1 - c^{1/\mu})\cos(3\theta)\right]^{\mu}} \tag{16}$$

where exponent μ controls the convexity of the surface on the π-plane of the deviatoric stress ratio space. This μ is set fixed to 0.16 here, which provides convexity for the usual cases of $c > 0.67$. Observe here that $g = 1$ for $\theta = 0^{\mathrm{o}}$ and $g = c$ for $\theta = 60^{\mathrm{o}}$, thus rendering the pertinent values for the stress ratios in TC and TE on the basis of Eq. (15). The procuring shape of the three model surfaces (for $c = 0.712$) on the foregoing π-plane is shown in Fig. 1 for an exemplary case where $\psi < 0$, which dictates their apertures as a function of Eqs. (12) and (13).

2.4 Mapping rule

The distance of the current stress ratio $\boldsymbol{r}$ from these surfaces on the π-plane of the deviatoric stress ratio space is a key component of the constitutive equations. The distance from each surface is defined with the aid of the image points $\boldsymbol{r}^{\mathrm{c}}$,

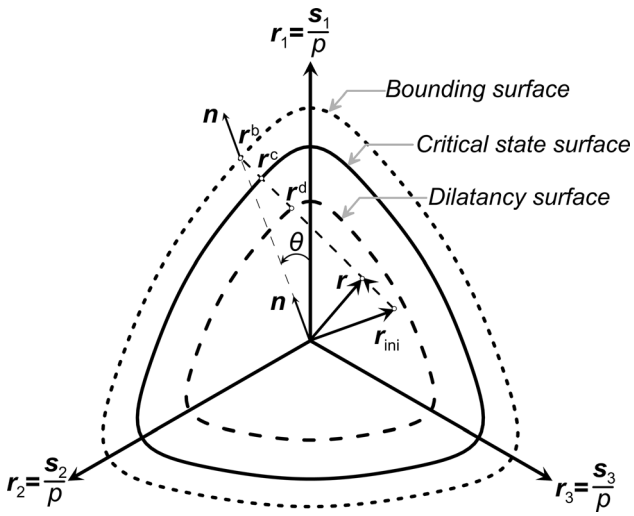

Fig. 1 Model surfaces on the π-plane of the deviatoric stress ratio space and adopted mapping rule. The relative location of dilatancy and bounding surfaces corresponds to a dilative state ($\psi < 0$)

$\boldsymbol{r}^{\mathrm{b}}$ and $\boldsymbol{r}^{\mathrm{d}}$ (collectively $\boldsymbol{r}^{\mathrm{c,b,d}}$) of $\boldsymbol{r}$ on the critical state, the bounding and the dilatancy surfaces, respectively. These image points are defined on the basis of the selected mapping rule, which is schematically illustrated in Fig. 1. This radial mapping rule has been repeatedly used in the past (e.g., [1, 68]).

The all-important tensor $\boldsymbol{r}_{\mathrm{ini}}$ refers to the tensor $\boldsymbol{r}$ when the last load reversal took place, i.e., when the loading index Λ of Eq. (6) or Eq. (9) took a negative value last. For the first shearing path, it is, by default, equal to the value of tensor $\boldsymbol{r}$ at the initial state (e.g., end of consolidation). This correlation to the recent shear history via $\boldsymbol{r}_{\mathrm{ini}}$ dates back to the concept of stress reversal surfaces by Mróz et al. [39] and Mróz and Zienkiewicz [38]. Having determined the image point $\boldsymbol{r}^{\mathrm{b}}$ on the bounding surface allows for the definition of the unit-norm deviatoric tensor $\boldsymbol{n}$ starting from the stress origin and depicting its direction as:

$$\boldsymbol{n} = \frac{\boldsymbol{r}^{\mathrm{b}}}{\sqrt{\boldsymbol{r}^{\mathrm{b}} : \boldsymbol{r}^{\mathrm{b}}}} \tag{17}$$

Given the unit-norm tensor $\boldsymbol{n}$, the image points on all three model surfaces may be computed as:

$$\boldsymbol{r}^{\mathrm{c,b,d}} = \sqrt{\frac{2}{3}} M_{\theta}^{\mathrm{c,b,d}} \boldsymbol{n} \tag{18}$$

where $M_{\theta}^{\mathrm{c,b,d}}$ is defined in Eq. (15). Consequently, the scalar distance between the current stress ratio $\boldsymbol{r}$ and the model surfaces (collectively $d^{\mathrm{c,b,d}}$) is computed along the $\boldsymbol{n}$ direction, as:

$$d^{\mathrm{c,b,d}} = (\boldsymbol{r}^{\mathrm{c,b,d}} - \boldsymbol{r}) : \boldsymbol{n} \tag{19}$$

According to Eq. (19), a positive $d^{\mathrm{c,b,d}}$ value implies a current stress ratio $\boldsymbol{r}$ located inside the corresponding surface, while a negative value of the distance $d^{\mathrm{c,b,d}}$ depicts that it is outside.

2.5 Elastic moduli

The maximum value of the shear modulus $G_{\max}$ used herein follows a hypoelastic formulation, since it is a function of the current values of the mean effective stress p and the void ratio e. Specifically, based on Hardin [21], it holds:

$$G_{\max} = G_{\mathrm{o}}\, p_{\mathrm{atm}} \left(\frac{1}{0.3 + 0.7e^2} \right) \sqrt{\frac{p}{p_{\mathrm{atm}}}} \tag{20}$$

where G_{o} is a model parameter and p_{atm} is the atmospheric pressure. However, the tangential value of the shear modulus G_{t} entering the calculation of the elastic strain rate (see Eq. (3)) incorporates a Ramberg–Osgood-type ([48]) hysteretic behavior, which provides a nonlinear degradation with strain. This concept, originally proposed by Papadimitriou et al. [43] and then used slightly modified by Andrianopoulos et al. [1], Loukidis and Salgado [33] and Taborda et al. [55], allows for a smooth decrease in the tangential shear modulus G_{t}, from its maximum value (equal to $G_{\max}$ from Eq. (20)) and a consequent smooth increase in hysteretic damping with increasing shear amplitude (e.g., [67]). In more detail, the nonlinear hysteretic form of G_{t} is given as:

$$G_{\mathrm{t}} = \frac{G_{\max}}{T} \tag{21}$$

where T is a positive scalar (≥ 1) variable, defined as:

$$T = 1 + 2\left(\frac{1}{a_1} - 1\right) \left(\frac{\sqrt{\frac{1}{2}(\boldsymbol{r} - \boldsymbol{r}_{\mathrm{ini}}) : (\boldsymbol{r} - \boldsymbol{r}_{\mathrm{ini}})}}{a_1 \left(\frac{G_{\max}}{p}\right) \gamma_1} \right) \tag{22}$$

Respectively, the tangential bulk modulus K_{t} entering Eq. (3) is interrelated to the tangential shear modulus G_{t} on the basis of a constant value v of the Poisson's ratio (a model parameter) according to:

$$K_{\mathrm{t}} = \frac{2}{3} \frac{(1+v)}{(1-2v)} G_{\mathrm{t}} \tag{23}$$

Note that according to Eq. (22) variable T reduces the shear modulus G_{t} as the current deviatoric stress ratio $\boldsymbol{r}$ diverts from the stress ratio $\boldsymbol{r}_{\mathrm{ini}}$ at the last stress reversal. In comparison with the Andrianopoulos et al. [1] version of variable T, the first difference is that in its denominator the current values of $G_{\max}$ and p are used and not those at the last stress reversal (the same was also assumed in [33]). The second difference is the use of a_1 (≤ 1) and γ_1 (> 0) as fixed constants here, and not as model parameters that is the common choice in practically all pertinent formulations in the literature (e.g., [1, 33, 43, 55]). The hereby adopted fixed values are $a_1 = 0.85$ and $\gamma_1 = 0.03\%$, i.e., they correspond to the upper bound of the range originally proposed by Papadimitriou et al. [43]. Fixing these parameters provides user-friendliness, but obviously reduces the flexibility of the model. However, extensive verification against data from multiple sands has shown that the plastic formulation of the model (described in the sequel) is flexible enough to provide the remainder of the measured nonlinearity.

It has to be underlined here that without the additional nonlinearity offered by variable T it is impossible to attain accurate simulations across the whole range of shear strains, from small–strain dynamic loading to large-strain monotonic shearing using the same set of model parameters, with the $G_{\max}$ being calibrated from truly small-strain measurements (e.g., bender elements, geophysical measurements). Another significant contribution of this formulation was highlighted in Loukidis and Salgado [33],

where it was shown that without variable T it is impossible to obtain compatible drained and undrained stress–dilatancy response while retaining realistic values of Poisson's ratio v and G_{max} irrespective of type of loading.

2.6 Plastic modulus

The plastic modulus K_p in Eq. (6) is given by:

$$K_p = h_o\, h_\theta\, h_f\, h_{pp}\, h_{ep}\, p\, \frac{d^b}{(\boldsymbol{r}-\boldsymbol{r}_{ini}):\boldsymbol{n}} \tag{24}$$

where h_θ, h_f, h_{pp}, h_{ep} are nonnegative model functions that will be discussed extensively in the sequel, and h_o a nonnegative model parameter. Based on Eq. (24), the sign of plastic modulus K_p is controlled by the sign of the distance d^b. According to Eq. (6), when $\Lambda > 0$, hardening response occurs when the $\boldsymbol{r}$ lies inside the bounding surface ($d^b > 0$), or, on the contrary, softening response occurs when the $\boldsymbol{r}$ lies outside the bounding surface ($d^b < 0$). Moreover, the denominator $(\boldsymbol{r}-\boldsymbol{r}_{ini}):\boldsymbol{n}$ implies that at the initialization of a load reversal (where $\boldsymbol{r}_{ini}$ has just been updated to the value of $\boldsymbol{r}$) the K_p takes an infinite value, thus leading to zero plastic strain at the beginning of every new shearing process.

Next, the effects of mean effective stress p and void ratio e on the K_p, that are introduced via functions h_{pp} and h_{ep} respectively, will be discussed. Specifically, function h_{pp} is given by:

$$h_{pp} = \sqrt{\frac{p_{atm}}{p}} \tag{25}$$

which, in combination with p multiplying the right part of Eq. (24), results in a total effect of mean effective stress on K_p having an exponent of 0.5, in agreement with Eq. (20) for the elastic moduli. Note that in constitutive models for sands, the selected value of 0.5 for this exponent is the most common choice, although there are models in which this exponent reaches 1.5 (e.g., [55]). Similarly, the decreasing effect of void ratio e on the plastic modulus K_p is introduced via:

$$h_{ep} = e^{-c_h} \tag{26}$$

where c_h is a nonnegative model parameter.

In the sequel, function h_θ introduces an additional effect of Lode angle θ on the plastic modulus. This is related to the need to show more compliant response in loading with intermediate θ values ($0^o < \theta < 60^o$), than what the $g(\theta,c)$ function of Eq. (16) provides in terms of the shape of model surfaces. For example, the comparison of resistance to liquefaction from cyclic triaxial tests (where angle θ jumps from 0° to 60°) versus that from cyclic simple shear tests (where angle θ takes intermediate values) shows that the former is larger than the latter (e.g., [40, 62]). Hence, here the function h_θ (≤ 1) is introduced as a multiplier of the K_p which reads:

$$h_\theta = [2g(\theta', c) - 1]^{5/2} \tag{27}$$

Function h_θ actually utilizes function g of Eq. (16) to capture the foregoing effect, but for a modified Lode angle $\theta' = \theta + 30^o$. In this way, for $\theta = 0^o$ (triaxial compression) and $\theta = 60^o$ (triaxial extension), the value of g entering Eq. (27) is the same and h_θ attains its maximum value. For intermediate values of θ, g attains lower values, resulting in lower values also for h_θ.

Finally, scalar-valued function h_f is a macroscopic index of the effects of fabric evolution on the sand response. The use of such fabric-related functions emphasizing on cyclic shearing effects is common practice in constitutive modeling (e.g., [1, 8, 12]). In this model, this significant effect on plastic strains is described macroscopically by the function h_f on K_p, which reads:

$$h_f = \frac{1 + \langle f_p - c_f \rangle^2}{1 + \langle \boldsymbol{f}_{ini}:\boldsymbol{n} \rangle} \tag{28}$$

Specifically, the h_f in Eq. (28) borrows elements of its formulation from the respective h_f functions of Papadimitriou and Bouckovalas [42] and Andrianopoulos et al. [1]. Specifically, the numerator is a quadratic function of scalar-valued variable f_p, while the denominator is a linear function of the inner product of an expression of a deviatoric fabric tensor $\boldsymbol{f}$ and the loading direction $\boldsymbol{n}$. In addition, both f_p and $\boldsymbol{f}$ initiate from zero at the initial state (leading to $h_f = 1$) and evolve independently with plastic volumetric strain, the latter only in dilation. Apart from these qualitative similarities to the h_f function in [42] and [1], in quantitative terms there are significant differences, since in the new model the evolution laws of f_p and $\boldsymbol{f}$ are as follows:

$$\dot{f_p} = (2-a) N\, h_{pf}\, \dot{\varepsilon}^p_{vol} \tag{29}$$

$$\dot{\boldsymbol{f}} = -N\, h_{post-liq} \left[\boldsymbol{f} + f_{max}^{(1+a)} \boldsymbol{n}\right] \langle -\dot{\varepsilon}^p_{vol} \rangle \tag{30}$$

where

$$N = N_o\, h_{ef}\, \langle -\psi_o \rangle^{0.1} \tag{31}$$

is the common evolution rate parameter for both f_p and $\boldsymbol{f}$, that is calibrated via N_o a nonnegative model parameter, that is the only parameter requiring calibration for function h_f. The above equations also include scaling functions that introduce effects of initial state on the evolution rate of both f_p and $\boldsymbol{f}$. Firstly, it is the effect of initial state parameter ψ_o, which appears in Macauley brackets that ensure a smooth transition between states where fabric evolution is important (when $\psi_o < 0$) and states where it is neglected (when $\psi_o > 0$), the latter mainly due to lack of pertinent experimental evidence. Then, the effects of the

initial values of mean effective stress p_o and void ratio e_o are included separately via:

$$h_{pf} = \left(\frac{p_{atm}}{p_o}\right)^{\frac{1}{2e_o^2}} \leq 1.5 \tag{32}$$

$$h_{ef} = e_o^{-0.5c_h} \tag{33}$$

Finally, note that parameters f_{max} and a that enter Eqs. (29) and (30) are variables that initiate from zero at the initial state and evolve during loading, as per:

$$f_{max} = \max(f_p) \tag{34}$$

$$0 \leq a = -2\left(\frac{|\int \dot{\varepsilon}_{vol}|}{|\int \dot{\varepsilon}_{vol}^{p}|} - 1\right) \leq 1 \tag{35}$$

where f_{max} is the maximum value that scalar f_p has taken during loading from the initial state, while a is a variable that takes values between 0.0 and 1.0, on the basis of the absolute values of 2 strain integrals measured during loading from the initial state: that of the total volumetric strain and that of the plastic volumetric strain.

Equations (28–35) constitute a complete framework for describing the effects of fabric evolution on the sand response. Function $h_{post\text{-}liq}$ entering Eq. (30) accounts for cyclic mobility and accumulation of strains after liquefaction is triggered, and its formulation is detailed in a special section below. For now, note that $h_{post\text{-}liq} = 1$ until initial liquefaction occurs, i.e., until the state when the current p becomes (for the first time) smaller or equal to a critical value $p_{l,}$ defined as $p_l = \min(0.05\ p_o; 10\ \text{kPa})$. In more detail, according to Eq. (29), function f_p in the numerator of h_f follows the whole shearing history of the sand, similarly to other models (e.g., [1, 42]). Model constant c_f and the inclusion of the $(f_p–c_f)$ difference into Macauley brackets in Eq. (28) imply that there is a threshold value of f_p, beyond which stiffening starts to affect the plastic modulus. This prevents stiffening during the early stages of monotonic shear loading, when the stress point remains inside the dilatancy surface, without essentially affecting cyclic loading in which the f_p surpasses quickly the value of c_f. A value of $c_f = 1$ is found appropriate for both monotonic and cyclic loading of various sands and is hereby adopted as a constant. Note that in existing similar models (e.g., [1, 42]), $c_f = 0$ holds.

At the same time, and according to Eq. (30), deviatoric fabric tensor $\boldsymbol{f}$ evolves only during dilation and not during the whole shearing history of the sand, i.e., unlike the f_p. During a dilative shear path, and due to the negative sign in the front of Eq. (30), the $\boldsymbol{f}$ develops in the opposite direction of the tensor quantity in brackets that is a function of the current values of the fabric tensor $\boldsymbol{f}$ and the loading direction $\boldsymbol{n}$. As such, in dilative shear paths the $\boldsymbol{f}$ may stop developing only if the tensor quantity in brackets becomes zero, which appears when the $\boldsymbol{f} = -f_{max}{}^{(1+a)}\boldsymbol{n}$, i.e., when the $\boldsymbol{f}$ takes its maximum norm, that is a nonnegative function (as f_p initiates from zero) of the maximum value that the f_p ever took during loading. However, it has to be underlined here that, unlike previous similar models (e.g., [1, 42]), it is not the value of fabric $\boldsymbol{f}$ that enters the h_f in Eq. (28), but the value of $\boldsymbol{f}_{ini}$, i.e., the value of fabric $\boldsymbol{f}$ at the last load reversal. In any case, based on Eq. (28), whenever the denominator of h_f takes values greater than 1.0, this leads to a decrease of K_p and hence a softening response is predicted. Such a softening response does not appear during monotonic loading (since $\boldsymbol{f}_{ini} = 0$), but only during unloading paths following loading outside the dilatancy surface.

Focusing on the common evolution rate parameter N for both f_p and $\boldsymbol{f}$, Eq. (31) incorporates its dependence on initial state. Particularly, function h_{ef} in Eq. (33), like its similar form included in the K_p equation (Eq. (26)), indicates a decreasing effect of (initial) void ratio on the rate of fabric evolution. Moreover, function h_{pf} (Eq. (32)) that multiplies N in Eq. (29) for the f_p evolution implies also a decreasing effect of (initial) mean effective stress on the rate of fabric evolution. Since the numerator of h_f (via the f_p evolution) mostly governs the stiffening response with cycles, the inclusion of functions h_{pf} and h_{ef} in the evolution of f_p in Eq. (29) ensures that the new model is in line with experimental results (e.g., [62]) and analytical relations (e.g., [22]) for the decreasing effect of overburden stress and relative density on the resistance to liquefaction via factor K_σ. This also explains the upper-bound value of 1.5 in h_{pf} of Eq. (32) in order to disallow excessive increase in liquefaction resistance for very small p_o values.

Gradual stiffening response with cycles is apparent both in drained and in early stages of undrained cyclic element tests. That is the reason why the accumulation of fabric-related components was conceptually chosen to develop with the plastic component of volumetric strain rate and not its total rate, similarly to all pertinent literature models (e.g., [1, 12]). However, this option creates an inherent quantitative differentiation of the fabric evolution under different drainage conditions. For example, if drainage occurs, the change of void ratio e directly affects the plastic modulus K_p via Eq. (26), and hence the value of the plastic volumetric strain rate entering fabric evolution via Eqs. (29) and (30). To counterbalance this effect, the intensity of fabric evolution during loading is set to depend on the correlation between the integral of the total volumetric strain and the integral of the plastic volumetric strain during loading via factor a that is introduced in Eq. (35) and takes values between 0.0 and 1.0. Based on its definition in Eq. (35), when the integral of total volumetric strain is equal to zero (e.g., in the extreme case of fully undrained conditions), then $a = 1.0$. On the other hand,

when the ratio of the volumetric strain integrals is greater than 1.0, i.e., when volume change is significant (e.g., in the case of fully drained conditions), then a = 0.0. For all the intermediate states, factor a attains values between 0.0 and 1.0 according to Eq. (35). Given the above definitions, the term $(2–a)N$ that acts as the scaling factor in Eq. (29) takes values between N and 2 N, while the maximum norm $f_{\max}{}^{(1+a)}$ that fabric tensor $\boldsymbol{f}$ may take in the bracketed tensor term of Eq. (30) takes values between $f_{\max}$ and $f_{\max}{}^{2}$.

It is understood that making fabric evolution partially a function of the integral of total volumetric strain via factor a may seem inconsistent. However, based on all the above, this integral affects merely the scaling factor of f_{p} evolution in Eq. (29) and the maximum norm of tensor $\boldsymbol{f}$ in Eq. (30). In other words, both f_{p} and $\boldsymbol{f}$ continue to evolve as functions of the plastic volumetric strain rate in Eqs. (29) and (30), and the role of factor a is merely to enhance or reduce fabric evolution effects on the plastic modulus K_{p} depending on whether the loading induces volume change or not. Such a factor does not appear in any previous similar model (e.g., [1, 12, 42]) that focused mostly on undrained loading (and liquefaction) and an example of its necessity for other than undrained conditions is discussed below. Specifically, Fig. 2 presents the predicted shear stress–strain (τ–γ_{SS}) relation and volumetric strain ($\varepsilon_{\mathrm{vol}}$–$\gamma_{\mathrm{SS}}$) accumulation within 30 cycles of a strain-controlled drained cyclic simple shear test with single amplitude cyclic shear strain equal to $\gamma_{\mathrm{SS,cyc}}$ = 0.1%. Subplots c and d include the model prediction having factor a varying according to Eq. (35), while subplots a and b present the same predictions but with a factor a = 1.0 that leads to the lowest f_{p} evolution rate equal to N and the highest maximum norm of $\boldsymbol{f}$ equal to $f_{\max}{}^{2}$. According to experimental evidence for drained cyclic loading (e.g., [51]), even for large cyclic shear strain amplitudes for which the shearing leads to dilation before the load reversal, the volumetric strain $\varepsilon_{\mathrm{vol}}$ accumulates with cycles, but at a steadily decreasing rate (e.g., see Fig. 2d), while the stress–strain relation becomes gradually stiffer (e.g., see Fig. 2c). In order to achieve this response, the new model (with variable a) employs f_{p} evolution rates higher than N, thus enhancing the numerator of h_{f}, concurrently with values of

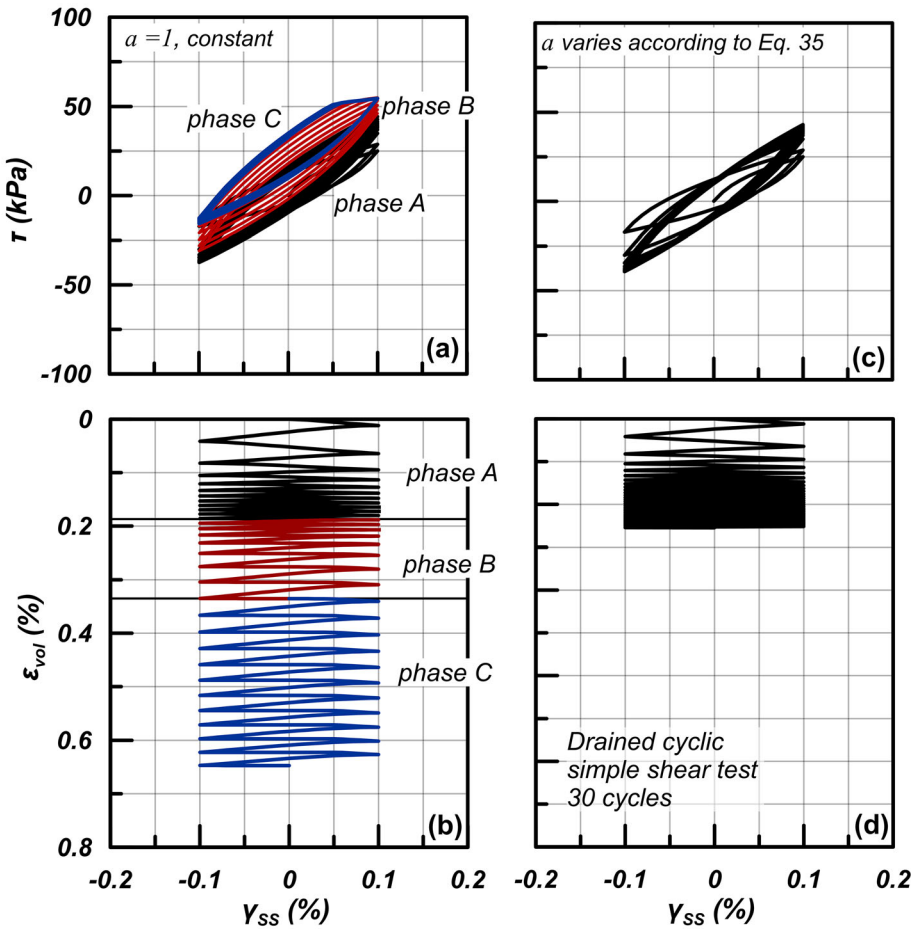

Fig. 2 Effect of factor a on the shear stress–strain (τ – γ_{ss}) relation and the volumetric strain ($\varepsilon_{\mathrm{vol}}$ – γ_{ss}) accumulation in 30 cycles of a strain-controlled drained cyclic simple shear test: **a** and **b** a = 1; **c** and **d** variable a, according to Eq. (35)

maximum norm of $\boldsymbol{f}$ lower than ${f_{\max}}^2$, thus reducing the importance of the denominator of h_f. As a result, the predicted response is a gradual stiffening with cycles due to the effect of a gradually increasing h_f.

On the contrary, using a constant value of $a = 1.0$ leads to a milder increase in the numerator of h_f concurrently with the potential for a more intense increase in its denominator. Such a choice may lead to the undesired response presented in Fig. 2a and b. Specifically, in the first cycles (phase A) the response becomes gradually stiffer, as it should. However, as the stress–strain loops become stiffer, the values of stress ratio $\boldsymbol{r}$ become higher and the stress point may shift outside the dilatancy surface. Due to the large maximum norm of ${f_{\max}}^2$, this partly dilative loading increases the $\boldsymbol{f}$ and thus the denominator of function h_f. As cyclic loading continues (phase B), the h_f gradually decreases, which leads to a softening response with cycles, i.e., an accelerated rate of ε_{vol} accumulation. This unrealistic softening leads to gradually larger ε_{vol} increments, which, in turn, allow for an intense evolution of the f_p and of the numerator of h_f. As a result, phase C of the loading appears, where the h_f increases and reduces equally within each cycle, thus leading to a constant rate of ε_{vol} accumulation with cycles, which is again unrealistic.

2.7 Dilatancy

According to Eq. (5), the definition of plastic strain rate direction $\boldsymbol{R}$ in this model implies non-associativity, since the scalar-valued dilatancy function D is explicitly defined. Specifically, the dilatancy D is hereby defined with different equations for the contractive and the dilative phases of loading, a concept not uncommon in constitutive modeling literature (e.g., see [8]).

2.7.1 Contraction

Plastic volumetric strains during contraction (i.e., when $d^d > 0$) are computed using the following expression for the dilatancy D:

$$D = A_o \frac{\left[(\boldsymbol{r} - \boldsymbol{r}_{ini}) : \boldsymbol{n} + \left\langle -d^d_{ini} \right\rangle\right]}{h_{pd,c}} d^d \tag{36}$$

where A_o is a nonnegative model parameter, while $h_{pd,c}$ is a nonnegative function related to the effect of mean effective stress p on the D for contractive states that will discussed in detail below. The correlation of D to the distance d^d implies that Eq. (36) is founded on a generalization of Rowe's dilatancy theory ([49]). However, the bracketed term in Eq. (36) includes the quantity $(\boldsymbol{r} - \boldsymbol{r}_{ini})$:$\boldsymbol{n}$, which becomes zero at each load reversal. At the same time, this bracketed term includes a quantity in Macauley brackets, which is related to the value of distance d^d at the last load reversal (depicted by d^d_{ini}) and is nonzero only when the last load reversal occurred outside the dilatancy surface ($d^d_{ini} < 0$). Hence, this bracketed term introduces the effect of the recent load reversal in the definition of D. This differentiation from Rowe's dilatancy theory implies $D = 0$ and $D \neq 0$ immediately after load reversal inside and outside the dilatancy surface, respectively. In all cases, as loading continues and the quantity $(\boldsymbol{r}–\boldsymbol{r}_{ini})$:$\boldsymbol{n}$ increases, the dilatancy D increases, before it eventually starts to decrease, as the effect of the decreasing d^d prevails when approaching the dilatancy surface where the $d^d = 0$, thus rendering $D = 0$, regardless of where the previous load reversal appeared.

Note here that the proposed Eq. (36) for D in contraction gives positive values of D close to zero for small values of quantity $(\boldsymbol{r}–\boldsymbol{r}_{ini})$:$\boldsymbol{n}$. This means that for cyclic loading in which this quantity remains generally small (e.g., for low amplitude cyclic loading), the D remains close to zero. This constitutive trait proves very useful for predicting minimal volume change under drained conditions, or minimal excess pore-pressure build-up under undrained conditions, when low amplitude cyclic loading is at hand, thus leading to relatively "*flat*" liquefaction resistance curves. Similar formulations for dilatancy (in contraction), that deviate from Rowe's dilatancy theory by introducing the distance from the last shear reversal $\boldsymbol{r}_{ini}$, can also be found in recent literature (e.g., [8, 10]). Alternatively, but aiming at the same target, Tsaparli et al. [61] included in the dilatancy function the ratio of the distance from the dilatancy surface over the value of the respective distance at the last shear reversal. Note also here that a term of similar functionality to the term in Macauley brackets in Eq. (36) was used also by Boulanger and Ziotopoulou [8], while reduced and nonzero initial value of D upon shear reversal is also predicted in Tsaparli et al. [61].

The last term to be discussed is the function $h_{pd,c}$ of Eq. (36), given as:

$$h_{pd,c} = \begin{cases} h_{pd,c}* & default \\ \min\left[h_{pd,c}*; \dfrac{h_{pd,c,liq}}{h_{pl,d}}\right] & after\ initial\ liquefaction \end{cases} \tag{37a}$$

with:

$$h_{pd,c}* = 1 - \langle sign(-\psi_o)\rangle \left[\left\langle 1 - \left(\frac{p}{p_o}\right)^{0.5} \right\rangle - c_{pd,c}\right] \tag{37b}$$

$$h_{pl,d} = \exp\left(-\left(\frac{p}{16p_l}\right)^4\right) \tag{37c}$$

Function $h_{pd,c}$ acquires a double form, depending on whether or not initial liquefaction has occurred. In its default form (before initial liquefaction), function $h_{pd,c} = h_{pd,c}^*$. This $h_{pd,c}^*$ function decreases from 1.0 as p decreases from its initial value p_o, thus leading to gradual increase of D as per Eq. (36). Due to the exponent 0.5, the foregoing decrease of $h_{pd,c}^*$ is notable only after a significant decrease of the p/p_o ratio (e.g., after significant excess pore-pressure build-up) and appears only for initially dilative initial states, i.e., only when the sign of $-\psi_o$ is positive, and hence, the $\langle sign(-\psi_o)\rangle = 1$. The inclusion of $c_{pd,c} = 0.1$ (i.e., a small positive number) guarantees that $h_{pd,c}^*$ remains positive and nonzero, when $p = 0$, while the Macauley brackets inside the bracketed term of Eq. (37b) make sure that for $p/p_o > 1$, the $h_{pd,c}^*$ remains constant and does not affect the response. Once initial liquefaction occurs for the first time, the value of $h_{pd,c}^*$ is stored as $h_{pd,c,liq}$. Thereafter, the value of $h_{pd,c}$ is estimated as the minimum of 2 values: the $h_{pd,c}^*$ on the basis of Eq. (37b) and the ratio of the aforementioned stored $h_{pd,c,liq}$ value over the function $h_{pl,d}$ of Eq. (37c) that introduces an effect of the p/p_l ratio. As a whole, Eq. (37) ensures that in contractive paths after initial liquefaction, the $h_{pd,c}$ remains lower than what the $h_{pd,c}^*$ prescribes and only when $p/p_l > 20$, approximately, the $h_{pd,c}$ becomes equal to $h_{pd,c}^*$ again, due to the operation of Eq. (37c).

2.7.2 Dilation

It has been made clear so far that in this model different dilatancy D functions are proposed for contraction ($d^d > 0$ and dilation ($d^d < 0$). However, it should be noted that during the transition from contractive to dilative stress state any discontinuity is prevented, as both D functions are proportional to d^d and thus, at the crossing point with the dilatancy surface $D = 0$ holds, due to $d^d = 0$.

During dilation, the dilatancy D takes the following form:

$$D = A_o \frac{2h_\theta}{h_{post-liq}\, h_{fd}} d^d \tag{38}$$

where A_o is the same model parameter as in Eq. (36), while h_θ is the function incorporating the loading direction (Lode angle θ) that is identical to that in Eq. (27), i.e., identical to that incorporated in the plastic modulus K_p equation. It is noted here that while in contraction the inclusion of the effect of h_θ only in K_p is proven sufficient, this effect is too subtle while in dilation, something that is especially true in monotonic loading. As also mentioned in the text explaining the K_p formulation, function $h_{post\text{-}liq}$ accounts for accumulation of strains after liquefaction is triggered, and its formulation is detailed in a following dedicated section. It suffices here to note that $h_{post\text{-}liq} = 1$ unless liquefaction occurs. Focusing on the form of Eq. (38), it is deduced that unlike Eq. (36), it adopts directly the essence of Rowe's dilatancy theory by defining a linear relation between D and d^d.

What remains is the explanation of the effect of fabric evolution on D in dilation that is introduced via function h_{fd}. Its inclusion in Eq. (38) stems from experimental observations in cyclic loading tests with very large cyclic shear amplitudes, in which net volume reduction is observed cycle after cycle, even if the stress state remains outside the dilatancy surface for significant portions of the loading (e.g., see drained cyclic experiments of [51]). This reduced tendency for dilation seems to appear gradually and is introduced via function h_{fd} according to:

$$h_{fd} = 1 + \langle f_{pd} - c_{fd} \rangle \tag{39}$$

where cumulative index f_{pd} initiates from $f_{pd} = 0$ at initial state and has an evolution equation that reads:

$$\dot{f}_{pd} = (1 - a) N\, h_{pf} \langle \dot{\varepsilon}_{vol}^p \rangle \tag{40}$$

Observe that scalar f_{pd} evolves only when the integrals of total and plastic volumetric strains have a comparable measure and hence $0 \le a < 1$ holds, as per Eq. (35), i.e., $\dot{f}_{pd} = 0$ in fully undrained conditions. In addition, note that its evolution is solely increasing, due to the inclusion of the plastic volumetric rate in Macauley brackets in Eq. (40). On the other hand, for small intensity cyclic loading which retains the stress state inside the dilatancy surface and dilation does not occur, the term h_{pd} plays no role. Finally, the inclusion of the (f_{pd}–c_{fd}) in Macauley brackets in Eq. (39), implies that a sufficiently large f_{pd} quantity should be accumulated, before the h_{fd} starts reducing the D in dilation. This essentially eliminates the h_{fd} effect in monotonic loading, which does not require any fabric-related function acting on D (e.g., [65]). For this purpose, a constant value of $c_{fd} = 3$ has been found suitable for all sands.

2.8 Post-liquefaction response and cyclic mobility

In recent years, within the framework of performance-based design, special research effort has been focused not only on liquefaction triggering, but also on the investigation of post-liquefaction deformations. There is a plethora of experimental evidence (e.g., [2, 4, 24, 71]) exhibiting significant shear strain accumulation after initial liquefaction, i.e., the state when the sand first reaches an excess pore pressure Δu that is at least 95% of the initial mean effective stress p_o, or equivalently when the mean effective stress p is smaller or equal to 5% of p_o. Capturing the

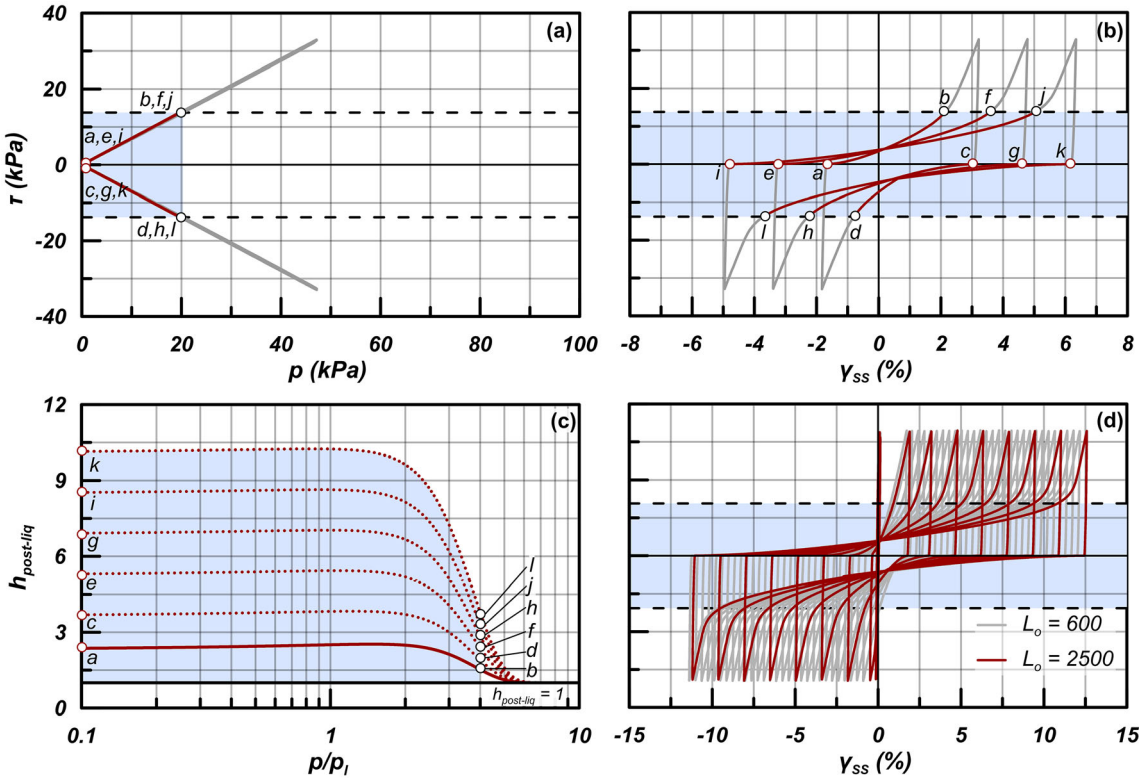

Fig. 3 **a** Typical overlaid effective stress path loops during cyclic mobility following initial liquefaction in undrained simple shear loading; **b** corresponding stress–strain loops with progressive shear strain accumulation with cycles; **c** evolution of function $h_{\text{post-liq}}$ as a function of p/p_{l} and **d** effect of model parameter L_{o} on post-liquefaction shear strain accumulation rate with cycles

Table 2 Values of model parameters for Toyoura sand and Ottawa-F65 sand

Constitutive part	Parameter	Values	
		Toyoura sand	Ottawa F-65 sand
Elasticity	G_{o}	650	400
	ν	0.15	0.15
CSL	e_{ref}	0.934	0.81
	λ	0.019	0.02
	ξ	0.70	0.75
	M_{c}^{c}	1.25	1.38
	c	0.712	0.74
Plastic modulus	n^{b}	1.1	0.7
	h_{o}	60	29
	c_{h}	12	8
Dilatancy	n^{d}	2	2
	A_{o}	1.5	2.4
Fabric	N_{o}	1550	600
Post-liquefaction	L_{o}	2500	5000

response after initial liquefaction has proven a challenge for constitutive models. To this extent, a variety of constitutive schemes has been proposed first by Elgamal et al. [20], then by Zhang and Wang [77], Boulanger and Ziotopoulou [8] and Tasiopoulou and Gerolymos [57], and very recently by numerous publications targeting this issue (e.g., [3, 10, 31, 74]). In this model, the cyclic mobility response is captured with the aid of function $h_{\text{post-liq}}$, primarily in Eq. (38) for the dilatancy D in dilation and secondarily in Eq. (30) for the evolution equation of the deviatoric fabric tensor $\boldsymbol{f}$ that affects the plastic modulus K_{p}. Specifically, the role of function $h_{\text{post-liq}}$ is to enable shear strain accumulation with cycles by (primarily) decreasing the dilation potential (via decreasing the D in dilation) after initial liquefaction in a progressive way, similarly to existing attempts in the literature (e.g., [8]). The target of this reduction of D is to avoid overlaid repeating stress strain loops during cyclic mobility. Here, this is achieved via a cumulative function varying continuously with mean effective stress p once initial liquefaction occurred, a concept originating from Barrero et al. [3]. This function, here, is given as:

$$h_{\text{post-liq}} = 1 + \left(2^{h_{\text{l}}} - 1\right) f_{\text{l}} \tag{41}$$

where f_{l} is a cumulative variable (initiating from $f_{\text{l}} = 0$), whose evolution equation reads:

$$\dot{f_l} = S\,L\,h_{pl}\left|\dot{\varepsilon}^{p}_{vol}\right| \tag{42}$$

with:

$$L = L_o\, e_o^{0.5c_h} \tag{43}$$

being the rate of its evolution, calibrated via L_o a non-negative model parameter and the void ratio e_o at initial state. Equations (41) and (42) include h_l and h_{pl}, two nonnegative functions of p, given by:

$$h_l = \exp\left(-\left(\frac{p}{4p_l}\right)^4\right) \tag{44}$$

$$h_{pl} = \exp\left(-\left(\frac{p}{10p_l}\right)^4\right) \tag{45}$$

Crucial for the evolution of f_l in Eq. (42) is S, i.e., a flag function with a default value of zero. This S is set equal to 1 only when initial liquefaction is reached for the first-time during loading, i.e., when the current p becomes smaller or equal to the critical value p_l. Based on the above, the f_l starts to accumulate via Eq. (42) only when the p becomes lower than p_l for the first time (due to switching to $S = 1$). The use of the absolute value of the plastic volumetric strain rate in Eq. (42) ensures that the f_l after initial liquefaction does not decrease, regardless of whether the sand experiences contraction or dilation. Of major importance in this f_l accumulation is the h_{pl} function which scales the rate of evolution L in Eq. (42). According to Eq. (45), the h_{pl} is a continuous nonlinear function of p/p_l with an upper limit equal to 1.0 (when the p approaches zero) and a lower limit of 0.0 (when the p has increased sufficiently beyond p_l). In essence, function h_{pl} allows for f_l accumulation only when the p is within a low effective stress regime and disallows it if the p becomes much larger, e.g., in the case of post-liquefaction re-consolidation. Such a p-dependence was recently introduced by Barrero et al. [3] and in the sequel by Yang et al. [74], who properly adjusted the plastic modulus and dilatancy functions when in this small p regime. Moreover, Cheng and Detournay [10] did the same for the adjustment of the plastic modulus. A p-dependence is also introduced on the $h_{post\text{-}liq}$ itself in Eq. (41), via function h_l in Eq. (44) that is very similar to the h_{pl} function of Eq. (45). This means that the $h_{post\text{-}liq}$ varies between 1.0 (when $h_l = 0.0$) and $(1 + f_l) > 1$ (when $h_l = 1.0$).

The operation of function $h_{post\text{-}liq}$ is discussed in Fig. 3 on the basis of the predicted response during cyclic mobility (following initial liquefaction) in undrained cyclic simple shear loading. The predictions are performed with the model parameters of Table 2 for Toyoura sand. Specifically, of interest is the response during the 3 overlaid effective stress path loops of this test shown in Fig. 3a, which correspond to the 3 non-overlaid stress–strain loops of increasing shear strain amplitude in Fig. 3b. Crucial in the successful simulation of this stress–strain response is the operation of $h_{post\text{-}liq}$, whose value during these 3 loading cycles is shown in Fig. 3c. Emphasis on the low mean effective stress p regime is provided via the shading, that depicts a range of $p < 20$ kPa and $p/p_l < 4$ (since p_l = 5 kPa for this example case). Observe in Fig. 3c that during the dilative phases of the loading cycles the $h_{post\text{-}liq}$ initiates from a set value (equal to $1 + f_l$) at $p \to 0$ (points a, c, e, g, i, k) and remains significantly larger than 1.0 only within the low stress regime, since the increase of p reduces the value of h_l in Eq. (44), thus leading to $h_{post\text{-}liq} = 1.0$ asymptotically, and this is regardless of the value of f_l in Eq. (41). However, the value of accumulated f_l increases cycle after cycle (due to the accumulation of plastic volumetric strain in Eq. (42) and so does the value of $(1 + f_l)$ from which initiates the $h_{post\text{-}liq}$ in each successive dilative phase (compare $h_{post\text{-}liq}$ values in paths a–b, c–d, e–f, g–h, i–j, k–l in Fig. 3c). Based on Eq. (38), these increased values of $h_{post\text{-}liq}$ lead to similarly decreased dilatancy D in successive dilative phases, which in turn lead to increased shear strains, especially in the low stress regime (compare range of γ_{SS} in paths a–b, c–d, e–f, g–h, i–j, k–l in Fig. 3b). Finally note that having the $h_{post\text{-}liq}$ multiplying the $\langle -\dot{\varepsilon}^{p}_{vol} \rangle$ term in the evolution of fabric tensor $\boldsymbol{f}$ in Eq. (30), essentially cancels out the post-liquefaction effect in the evolution of the fabric tensor $\boldsymbol{f}$, and through it, on the fabric evolution index h_f and the plastic modulus K_p. This ensures that during cyclic mobility the effective stress path loops remain essentially overlaid (see Fig. 3a), despite the shear strain accumulation exhibited by the stress–strain loops cycle after cycle (see Fig. 3b).

Moreover, Fig. 3d explores the effect of model parameter L_o that controls the rate of f_l accumulation via L, as per Eqs. (42) and (43). Observe that as the L_o increases, so does the rate of f_l accumulation, thus leading to larger $h_{post\text{-}liq}$ values and more intense shear strain accumulation. The value of rate L in Eq. (43) is also made a function of the void ratio at the initial state e_o, implying lower rates of post-liquefaction strain accumulation with an increase in relative density and the opposite, in accordance to data (e.g., [58]).

In closing, the formulation described above eventually leads to $h_{post\text{-}liq} = 1$ when a future loading process leads to values of p much larger than the p_l, i.e., outside the small p value regime related to liquefaction and cyclic mobility. In addition, if this future loading process leads to value of $p \geq p_o$ (e.g., re-consolidation after liquefaction), the model sets $f_l = 0$, i.e., it erases the memory of the preceding liquefaction. This approach is simple, but has a limitation with respect to what happens if this future loading process

increases the p, but to values lower than p_o or when this possible re-consolidation is followed by another liquefaction event in the future. The model unavoidably retains in memory the preceding liquefaction phase and hence the accumulated $f_l > 0$, something that may be potentially erroneous. To address such issues, an additional constitutive mechanism to eliminate and readjust this effect for subsequent totally different loading conditions, like in Barrero et al. [3], should be included, but such a complication is beyond the scope of this model.

2.9 Mitigation of the overshooting problem

This model employs the deviatoric stress ratio tensor at the last load reversal $\boldsymbol{r}_{\text{ini}}$ for defining a number of constitutive aspects, namely the loading direction tensor $\boldsymbol{n}$ (Fig. 1), the small-strain nonlinearity (Eq. 22), the plastic modulus (Eq. 24) and the dilatancy in contraction (Eq. 36). One of the problems faced in models employing the last load reversal point, or in models employing reversal surfaces in general, is the overshooting upon unloading and immediate reloading due to the updating of $\boldsymbol{r}_{\text{ini}}$ in both instances, i.e., the prediction of a stress–strain curve that is unrealistic since it overshoots the expected continuation that this curve would have if this unloading–reloading cycle had not occurred. In their recent work, Duque et al. [17] underlined the sensitivity of both advanced plasticity (e.g., bounding surface) and hypoplasticity models to this issue. This problem has been satisfactorily studied in the literature leading to several approaches for overcoming it (e.g., [8, 10, 11, 14, 27, 76]). In this model, the problem is more complicated, since also the loading direction tensor $\boldsymbol{n}$ may be affected, while the dilatancy is updated as well. So, the issue here is not just an overshooting problem, and in terms of constitutive modeling, it boils down to what is the "*accurate*" value of $\boldsymbol{r}_{\text{ini}}$ for having a realistic response in any load path that may be encountered in boundary value problems, both static and dynamic.

As a first step, here the approach of Dafalias and Taiebat [14] is adopted, i.e., a robust methodology for "*adjusting*" the value of $\boldsymbol{r}_{\text{ini}}$ depending on the load path. In order to understand their methodology, the following terms are defined: $\boldsymbol{r}^{(\text{m})}$ is the current stress ratio tensor along the current load path (m) at the moment of load reversal (i.e., when $A < 0$ appears), $\boldsymbol{r}_{\text{ini}}^{(\text{m})}$ refers to the $\boldsymbol{r}_{\text{ini}}$ adopted at the initiation of load path (m), $\boldsymbol{r}_{\text{ini}}^{(\text{m}-1)}$ is the $\boldsymbol{r}_{\text{ini}}$ of the previous load path (m-1) and $\boldsymbol{r}_{\text{ini}}^{(\text{m}+1)}$ refers to the $\boldsymbol{r}_{\text{ini}}$ that is going to be adopted after the initiation of the upcoming (m + 1) load path. When $A < 0$ appears during load path (m), the $\boldsymbol{r} = \boldsymbol{r}^{(\text{m})}$ and the quandary is whether $\boldsymbol{r}_{\text{ini}}^{(\text{m}+1)}$ should be updated to $\boldsymbol{r}^{(\text{m})}$, thus increasing the stiffness of the stress–strain curve during the upcoming path (m + 1), or whether it should take another value. According to Dafalias and Taiebat [14] the answer depends on the "*magnitude*" of load path (m), that is quantified in terms of $e^{\text{p(m)}}$, the integral of plastic deviatoric strain quantity $\sqrt{(2/3)\dot{\boldsymbol{e}}^{\text{p}} : \dot{\boldsymbol{e}}^{\text{p}}}$ during this path. For intermediate values of $e^{\text{p(m)}}$ an interpolation function for $\boldsymbol{r}_{\text{ini}}^{(\text{m}+1)}$ should be used, which according to Dafalias and Taiebat [14] reads:

$$\boldsymbol{r}_{\text{ini}}^{(\text{m}+1)} = k\,\boldsymbol{r}_{\text{ini}}^{(\text{m}-1)} + (1 - k)\boldsymbol{r}^{(\text{m})} \tag{46}$$

$$k = \left\langle 1 - \left(\frac{e^{\text{p(m)}}}{e_1^{\text{p}}} \right)^{n} \right\rangle \tag{47}$$

where k is the weighting parameter of Eq. (46) that quantifies the significance of load path (m) on the basis of the relative magnitude of plastic deviatoric strain $e^{\text{p(m)}}$ in comparison with e_1^{p}, a model constant serving as a shear strain threshold beyond which $\boldsymbol{r}_{\text{ini}}^{(\text{m}+1)} = \boldsymbol{r}^{(\text{m})}$. In this model, $\boldsymbol{e}_1^{\text{p}} = 10^{-4}$, and n, the model constant controlling the nonlinearity of Eq. (47), is set equal to 1, following the advice of Dafalias and Taiebat [14] for both. Based on the above, during any load path (m), both $\boldsymbol{r}_{\text{ini}}^{(\text{m}-1)}$ and $\boldsymbol{r}_{\text{ini}}^{(\text{m})}$ should be kept into memory, the former for use in Eq. (46), while the latter as the $\boldsymbol{r}_{\text{ini}}$ entering all aspects of the constitutive model presented above.

According to Eqs. (46) and (47), if load path (m) is negligible in terms of $e^{\text{p(m)}}$, then $\boldsymbol{r}_{\text{ini}}^{(\text{m}+1)} = \boldsymbol{r}_{\text{ini}}^{(\text{m}-1)}$ (due to $k = 1$) and for loading path (m + 1), only $\boldsymbol{r}_{\text{ini}}^{(\text{m})}$ and $\boldsymbol{r}_{\text{ini}}^{(\text{m}+1)}$ are kept into memory, while the all-important $\boldsymbol{r}_{\text{ini}}^{(\text{m}-1)}$ is erased from memory. This is fine if loading path (m + 1) is significant. If it is not and $k = 1$ holds again, then, ideally, the $\boldsymbol{r}_{\text{ini}}^{(\text{m}+2)}$ should be again equal to $\boldsymbol{r}_{\text{ini}}^{(\text{m}-1)}$, only that this value has been erased from memory. This loss-of-memory problem does not only appear when $k = 1$, but also for $0 < k < 1$, only that it requires a number of successive negligible load paths to erase from memory the effect of the all-important $\boldsymbol{r}_{\text{ini}}^{(\text{m}-1)}$. Such paths with successive negligible load paths are not uncommon in boundary value problems, especially of dynamic nature. This shortcoming is hereby remedied, by supplementing the foregoing methodology with a criterion on whether a load reversal (a state where $A < 0$) is "*formal*" or "*informal.*" Namely, as soon as a load reversal is detected for the initiation of load path (m + 1) at $\boldsymbol{r} = \boldsymbol{r}^{(\text{m})}$, it is considered by default "*informal*" and no update of $\boldsymbol{r}_{\text{ini}}$ is performed (i.e., $\boldsymbol{r}_{\text{ini}} = \boldsymbol{r}_{\text{ini}}^{(\text{m})}$ remains). This holds until the accumulated stress ratio difference from the "*informal*" load reversal point is larger than a preset (small) tolerance level r_{tol}. If this occurs, then the load reversal point is considered "*formal*" and the

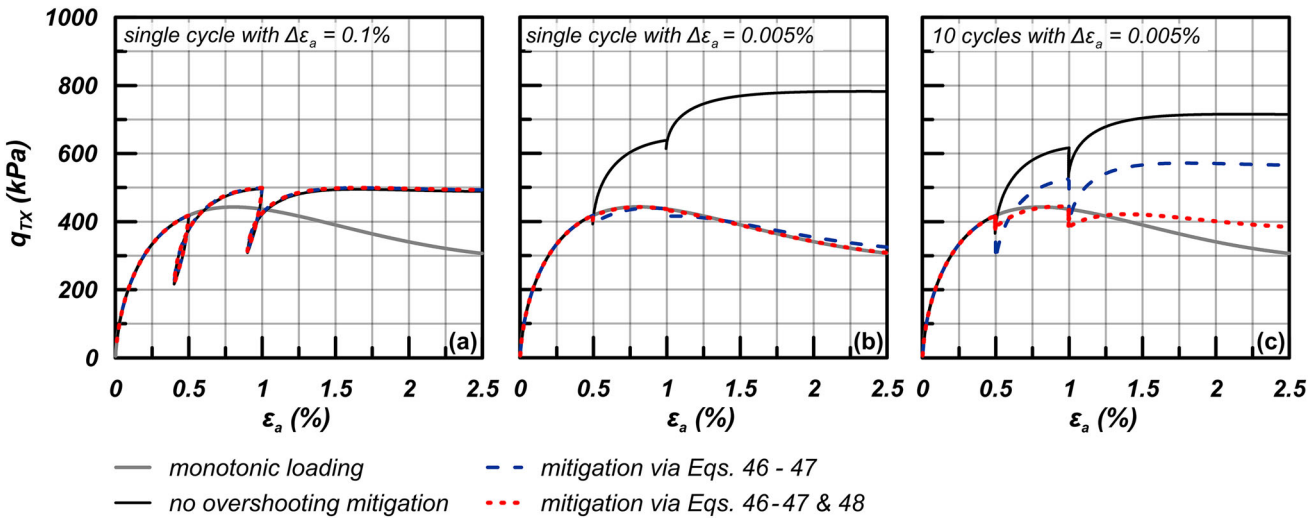

Fig. 4 Performance of different schemes to treat overshooting for the stress–strain response of an undrained triaxial compression test, with three different cases of unloading–reloading cycles at $\varepsilon_a = 0.5\%$ and 1.0%: **a** single cycle with $\Delta\varepsilon_a = 0.1\%$, **b** single cycle with $\Delta\varepsilon_a = 0.005\%$, **c** 10 successive cycles with $\Delta\varepsilon_a = 0.005\%$

estimation of the $\boldsymbol{r}_{\text{ini}}^{(\text{m}+1)}$ is performed on the basis of Eqs. (46) and (47). In more detail, the condition that should be satisfied for considering the last load reversal as "*formal*" reads:

$$\sqrt{(2/3)(\boldsymbol{r}-\boldsymbol{r}^{(\text{m})}):(\boldsymbol{r}-\boldsymbol{r}^{(\text{m})})} \geq r_{\text{tol}} \tag{48}$$

where r_{tol} is a model constant selected equal to 0.01 here. During the (small) loading path following an "*informal*" load reversal that has not updated the $\boldsymbol{r}_{\text{ini}}$, the loading index Λ usually continues to be negative, and thus, only elastic deformations are developed.

In Fig. 4, the effectiveness of this enhanced methodology for mitigating overshooting is presented for an exemplary case of an undrained triaxial test (for $p_o = 1000$ kPa and $e_o = 0.870$) that is simulated with the model parameters of Table 2 for Toyoura sand. The test is not monotonic, since when the axial strain becomes equal to $\varepsilon_a = 0.5\%$ and 1%, three different cases of unloading–reloading are imposed, as depicted in subplots a, b and c. Specifically, in Fig. 4a, a single strain-controlled cycle with a large $\Delta\varepsilon_a = 0.1\%$ is applied at both levels of ε_a, while in Fig. 4b this single cycle has a much smaller strain amplitude of $\Delta\varepsilon_a = 0.005\%$. Finally, in Fig. 4c, at both levels of ε_a, 10 successive cycles with $\Delta\varepsilon_a = 0.005\%$ are applied. In all subplots, the curve of the reference monotonic test is included, but this may only be considered relevant in Fig. 4b and 4c where the applied unload–reload cycles are of very small-strain amplitude. On top of this monotonic test curve, in all subplots, three stress–strain curves of the actual test are compared: one without mitigating overshooting, one that employs only Eqs. (46) and (47), and one that employs the whole methodology (including Eq. (48)). It is concluded that overshooting correction is not needed when the unload–reload cycles are of large amplitude (Fig. 4a). However, it is also shown that the overshooting correction of Dafalias and Taiebat [14], i.e., Eqs. (46) and (47), is required when the unload–reload cycles are of small amplitude (Fig. 4b), with the addition of Eq. (48) proving necessary for the more general case of multiple cycles of small amplitude (see Fig. 4c). In closing, note that the large differences in the stress–strain response with and without overshooting mitigation shown in Fig. 4 (e.g., increase of q_{TX} by more than 100% for $\varepsilon_a = 2\%$ in Fig. 4b) should be viewed as an upper-bound estimate. For fully drained conditions and/or a more dilative initial state, the differences would be smaller, yet they would still vouch for the need of stress–strain overshooting mitigation.

3 Calibration procedure of model parameters

The proposed model requires the calibration of 14 parameters. Their values for Toyoura and Ottawa-F65 sand are summarized in Table 2.

They are divided in different groups according to the constitutive part they refer to. Of these 14 model parameters, 2 are related to elasticity, 5 to critical state, 3 to the plastic modulus, 2 to the dilatancy, 1 to fabric evolution and 1 to post-liquefaction response. The procedure of determining their values will be discussed here using Toyoura sand as merely an example case. As described in the previous section, the present model has similarities with the models proposed by Papadimitriou and Bouckovalas

[42], Andrianopoulos et al. [1], Dafalias and Manzari [12] and Taiebat and Dafalias [56]. Their common constitutive ingredients include model parameters, whose calibration rationale is adopted unchanged and need not be repeated. This is the case for the first 12 out of the 14 model parameters in Table 2, i.e., the model parameters referring to elasticity, critical state, plastic modulus and dilatancy. It is merely mentioned here that out of these 12 model parameters, only 3 of them (h_o, c_h and A_o) require trial-and-error runs, while the remaining 9 parameters may be directly measured or estimated (e.g., for Toyoura sand: $M_c^c = 1.25$, $c = 0.712$, as in [12]; $e_{cs} = 0.934$, $\lambda = 0.019$, $\xi = 0.70$ as in [28]; $\nu = 0.15$ in accordance with [52] and [59]).

The exception to the foregoing rule is elastic parameter G_o that quantifies the elastic shear modulus (G_{max}), which must always be calibrated against small-strain tests (e.g., bender elements, resonant column tests), or wave propagation tests in the field or laboratory. According to McAllister et al. [37], the use of conventional triaxial data for this purpose (as is often performed in the literature) may lead to underestimation of its value. Here, the data of Wicaksono and Kuwano [70] for Toyoura sand are used for this purpose. As shear modulus was measured through different dynamic methods (trigger accelerometer, bender element, plate transducer), an average value is considered for the calibration of G_o. In Fig. 5, the comparison between the measured and predicted (by Eq. (20)) elastic small-strain shear modulus G_{max} is presented, for the selected value of $G_o = 650$. The comparison is made in terms of G_{max} versus mean effective stress p, for three different values of void ratio ($e = 0.811$-$D_r \approx 45\%$; $e = 0.756$-$D_r \approx 60\%$; $e = 0.700$-$D_r \approx 75\%$). Based on the good fitting of the data in Fig. 5, apart from the appropriate G_o value, the calibrated Eq. (20) predicts quite well the correlation of G_{max} with relative density and stress level.

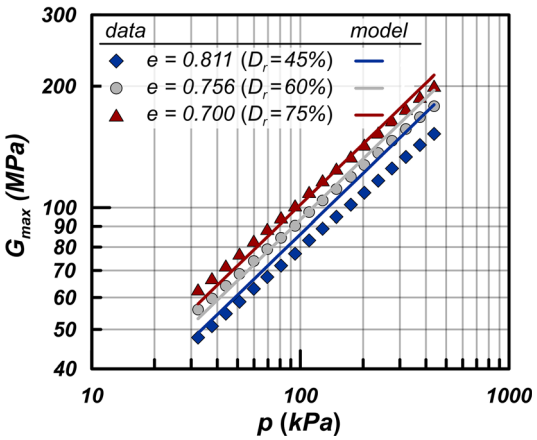

Fig. 5 Comparison of predicted G_{max} values versus their measurements by Wicaksono and Kuwano [70] as a function of void ratio e and mean effective stress p, after calibration of parameter G_o for Toyoura sand

The remaining 2 model parameters determine the cyclic response and are estimated on the basis of cyclic tests at the end of the calibration process, i.e., after the first 12 model parameters. The fabric evolution intensity constant N_o is calibrated by trial-and-error runs that target either the accumulated volumetric strains during cyclic drained tests, or the number of cycles to reach initial liquefaction during cyclic undrained tests. The selection of type of cyclic tests to be used depends on availability, or the task at hand, but both can be used equally well. Figure 6 illustrates the key role of N_o in controlling the intensity of fabric evolution function h_f, Eq. (28), in 4 indicative loading conditions: 2 under cyclic (subplots a, c) and 2 under monotonic conditions (subplots b, d). In Fig. 6a, the effective stress path of a cyclic undrained triaxial test shows how the parameter N_o can be used to adjust the predicted rate of excess pore-pressure build-up and the number of cycles until initial liquefaction is triggered. Model predictions are compared with an undrained cyclic triaxial test performed by Toyota and Takada [60] ($e = 0.756$ ($D_r \approx 60\%$), $p_o = 98.1$ kPa). In the same way, in Fig. 6c the effect of N_o on the rate of accumulation of volumetric strains during a drained cyclic simple shear test-with the same initial conditions, but now with $K_o = 0.50$ instead of 1.0 - is explored. For this type of loading, experimental data for Toyoura sand are not available, but at least the accumulation of volumetric strains is validated against the empirical estimate of Duku et al. [16]. Moreover, Fig. 6b and 6d compares model predictions to monotonic triaxial compression tests of Verdugo and Ishihara [65] (Fig. 6b-undrained test with $e = 0.833$ ($D_r \approx 37\%$), $p_o = 100$ kPa; Fig. 6d-drained test with $e = 0.831$ ($D_r \approx 37\%$), $p_o = 100$ kPa). These comparisons with monotonic test data show that the fabric evolution function affects only marginally the monotonic response, but is crucial for a satisfactory cyclic loading prediction. Hence, the calibration for monotonic tests may be performed for $N_o = 0$, and then, the final value of N_o can be calibrated on the basis of trial-and-error simulations of cyclic tests, without essentially deteriorating the predicted monotonic response.

The last model parameter L_o requiring calibration is linked to the post-liquefaction shear strain accumulation and is quantified also by a trial-and-error procedure. It controls the intensity of the dilatancy decrease in dilation after initial liquefaction occurs, and thus the rate of strain accumulation, as depicted in Fig. 3d. Note that its value has no effect on the pre-liquefaction phase and this is why it is calibrated last. Its calibration requires good quality cyclic undrained tests reaching well beyond initial liquefaction, thus allowing the estimation of the rate of strain

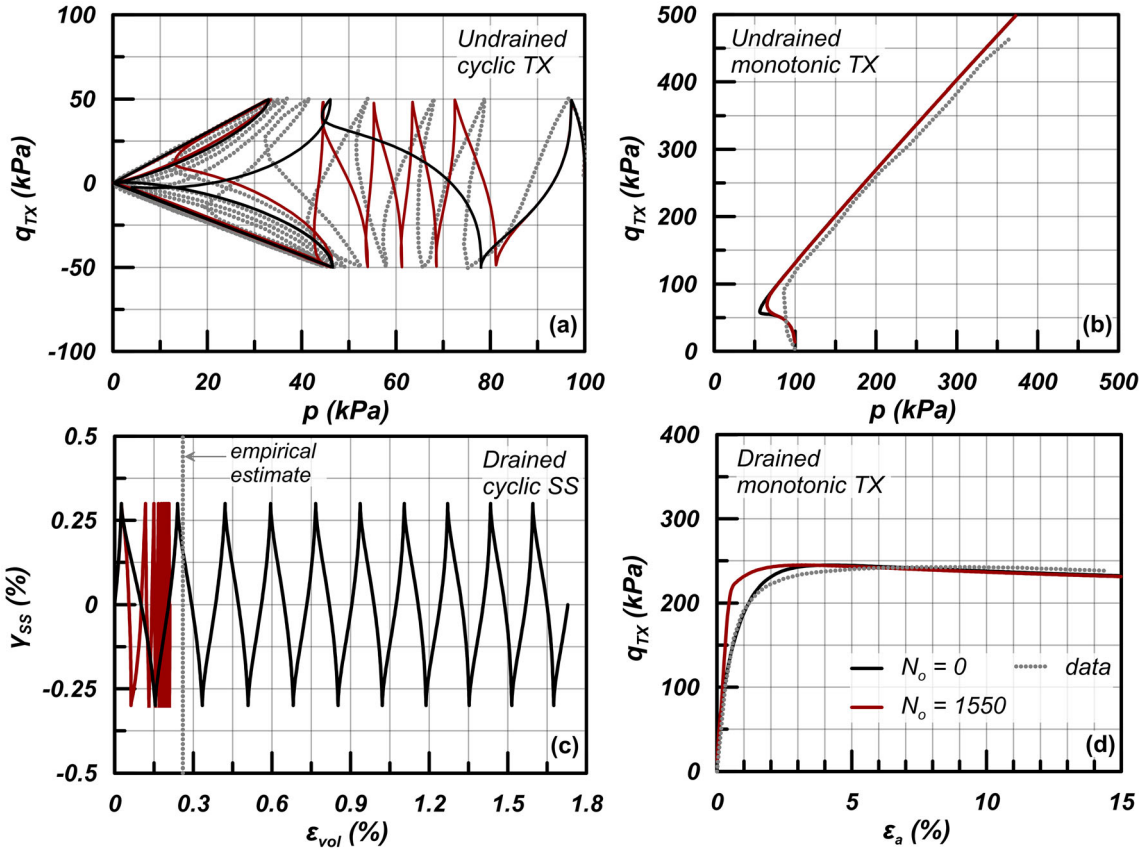

Fig. 6 Effect of fabric evolution function and its scaling parameter N_o on: **a** effective stress path during an undrained cyclic triaxial test; **b** effective stress path during an undrained monotonic triaxial compression test; **c** rate of accumulation of volumetric strain during a drained cyclic simple shear test; **d** stress–strain response during a drained monotonic triaxial compression test

accumulation thereafter. In absence of specific experimental data, the semiempirical framework of post-liquefaction shear deformation accumulation in sands, recently proposed by Tasiopoulou et al. [58], can prove useful for this purpose.

4 Model performance

In this section, the performance of the new model is evaluated. The validation includes simulations of both monotonic and cyclic shearing tests on Toyoura and Ottawa-F65 sand that were performed with the values of model parameters shown in Table 2. In order to present a thorough evaluation of model performance that addresses all important aspects of monotonic and cyclic response, wherever sand-specific data are lacking, the model performance is validated against empirical relations from the literature, especially for cyclic loading. In the following, each subsection illustrates a different type of loading and comparisons are presented for at least one of the two sands, if not for both. All the information regarding the characteristics of the element tests employed in this section is summarized in table format in Appendix.

4.1 Drained and undrained monotonic loading

The new model is used to simulate drained triaxial compression tests (TC) on Toyoura sand, performed by Verdugo and Ishihara [65] on isotropically consolidated samples. Figure 7 compares numerical simulations to experimental data in terms of (triaxial) deviatoric stress $q_{TX} = \sigma_a$-σ_r versus axial strain ε_a (subplots a, c) and volumetric strain ε_{vol} versus axial strain ε_a (subplots b, d). Subscripts a and r denote the axial and radial directions of the triaxial sample, respectively. Subplots a and b pertain to tests with p_o = 100 kPa, while subplots c and d to tests with p_o = 500 kPa, with p_o denoting the initial mean effective stress of the sample. The model simulates quite accurately the three distinct behaviors of the sand, as they emerge from the tests based on the initial value of void ratio e_o of the samples after consolidation. More specifically, stress-strain response and volumetric strain are properly predicted both in the cases of the dilative response

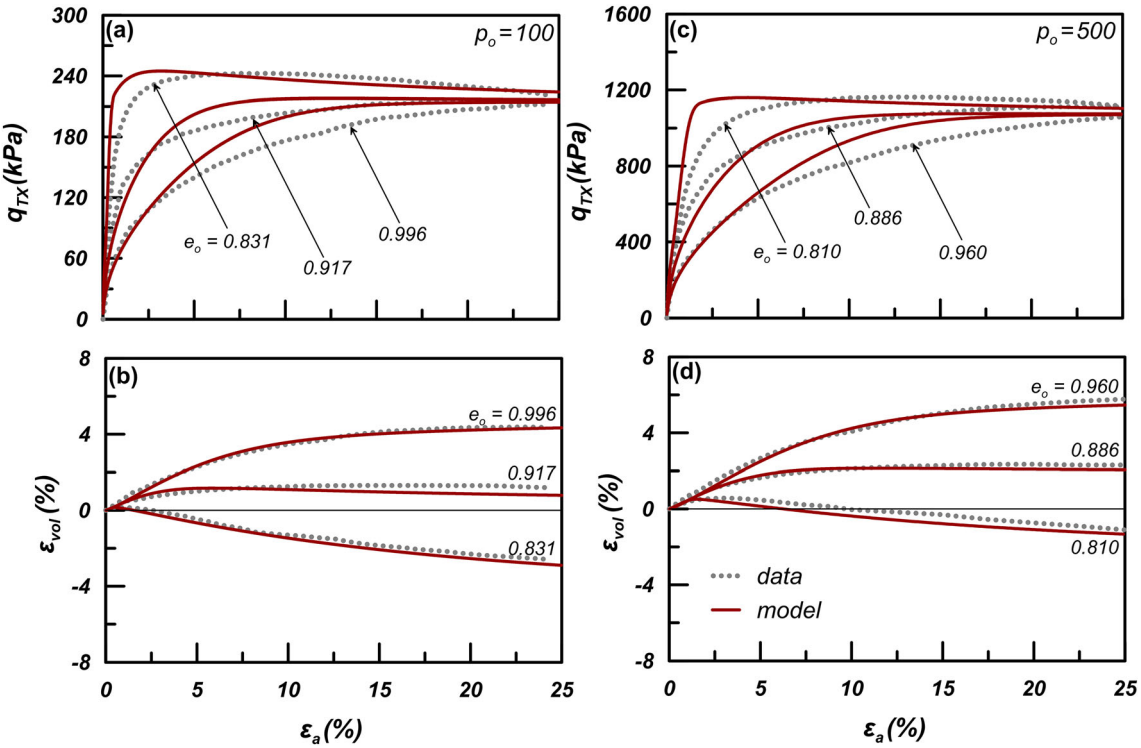

Fig. 7 Experimental results and model predictions of drained monotonic triaxial compression tests. Data on Toyoura sand after Verdugo and Ishihara [65]

of the medium–dense (e_o = 0.810-0.831, with D_r = 37-43%) samples, as well as the slightly (e_o = 0.886-0.917, with D_r = 14-23%) or intensively (e_o = 0.960-0.996, with D_r < 3%) contractive samples, for both stress levels.

In the sequel, the model performance is evaluated against the drained torsional shear tests (TS) of Pradhan et al. [47]. These torsional shear tests were performed after K_o-consolidation of the samples to an initial axial stress $\sigma_{a,o}$, and then, shear deformation is applied producing shear stress τ in the torsional shear apparatus, while retaining the effective axial stress constant ($\sigma_a = \sigma_{a,o}$). At the same time, radial and circumferential strain increments were kept equal to zero throughout the test, ensuring simple shear loading conditions. Three different combinations of initial axial stress $\sigma_{a,o}$ and initial void ratios e_o are presented. Based on Pradhan et al. [47], the K_o value in these samples is estimated by the empirical relation $K_o = 0.52e_o$ and the thus procuring values were considered in the simulations. In Fig. 8, the comparison of data to simulations is presented in terms of the stress ratio τ/σ_a versus shear strain $\gamma = \varepsilon_1 - \varepsilon_3$ (subplot a) and ε_{vol} versus γ (subplot b), where subscripts 1 and 3 denote the maximum and minimum principal values of the tensor, irrespective of its direction. The overall response is simulated with fair accuracy, besides the slight stiffer stress–strain response, mainly for the very dense sample with e_o = 0.674 (D_r = 81%).

Figure 9 shows the model performance for drained TC tests on Ottawa-F65 sand conducted by Vasko [63] and Vasko et al. [64] for medium–dense (e_o = 0.604, $D_r \approx$ 55%) and dense (e_o = 0.585, $D_r \approx$ 62%) isotropically consolidated samples. The comparison is presented in the format of Fig. 7. Three stress levels (100 kPa-300 kPa) are examined for each density. The comparison for e_o = 0.604 is quite satisfactory, while that for e_o = 0.585 is considered fair, with a slight under-prediction of the peak strength of these denser samples. For both relative densities, the volumetric response is predicted satisfactorily.

Subsequently, in Fig. 10, the model is evaluated against the undrained TC tests of Verdugo and Ishihara [65] on isotropically consolidated samples of Toyoura sand. The comparison of data versus simulations is shown in the spaces of q_{TX} versus ε_a (subplots a, c) and q_{TX} versus p (subplots b, d). The simulations concern two relative densities (e = 0.735 and 0.833, with $D_r \approx$ 63%-37%) and a great range of initial mean effective stresses, from p_o = 100 kPa to the extremely high value of p_o = 2000 kPa. Hence, the versatility of the model to predict both contractive or dilative response for this wide range of initial conditions, depending on the combination of e-p_o, is depicted.

Then, Fig. 11 compares experimental data to numerical simulations for undrained simple shear tests (SS),

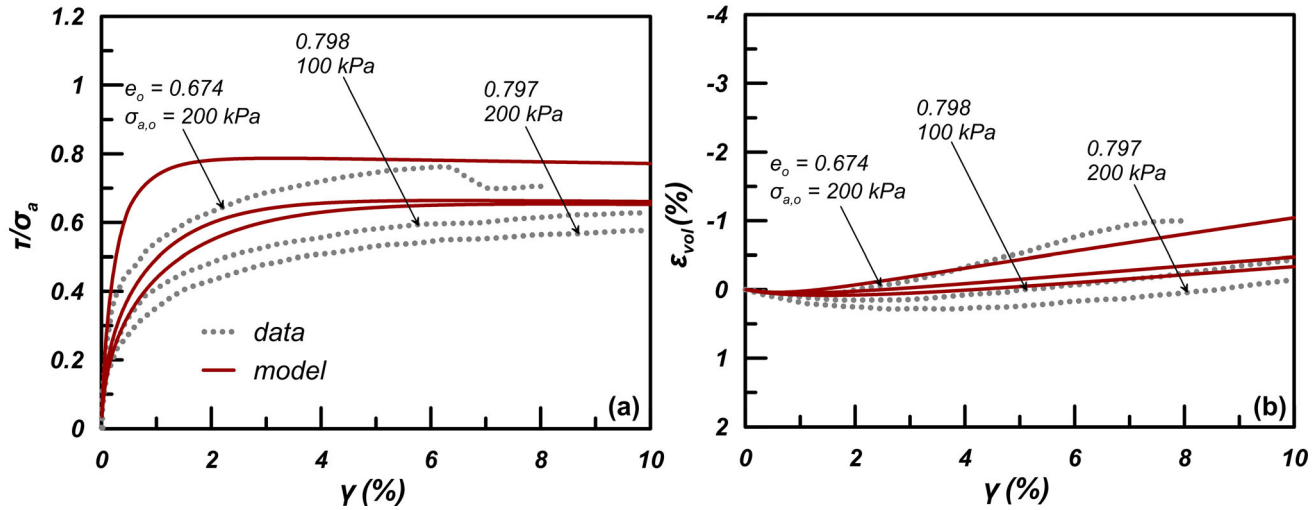

Fig. 8 Experimental results and model predictions of drained monotonic torsional shear tests. Data on Toyoura sand after Pradhan et al. [47]

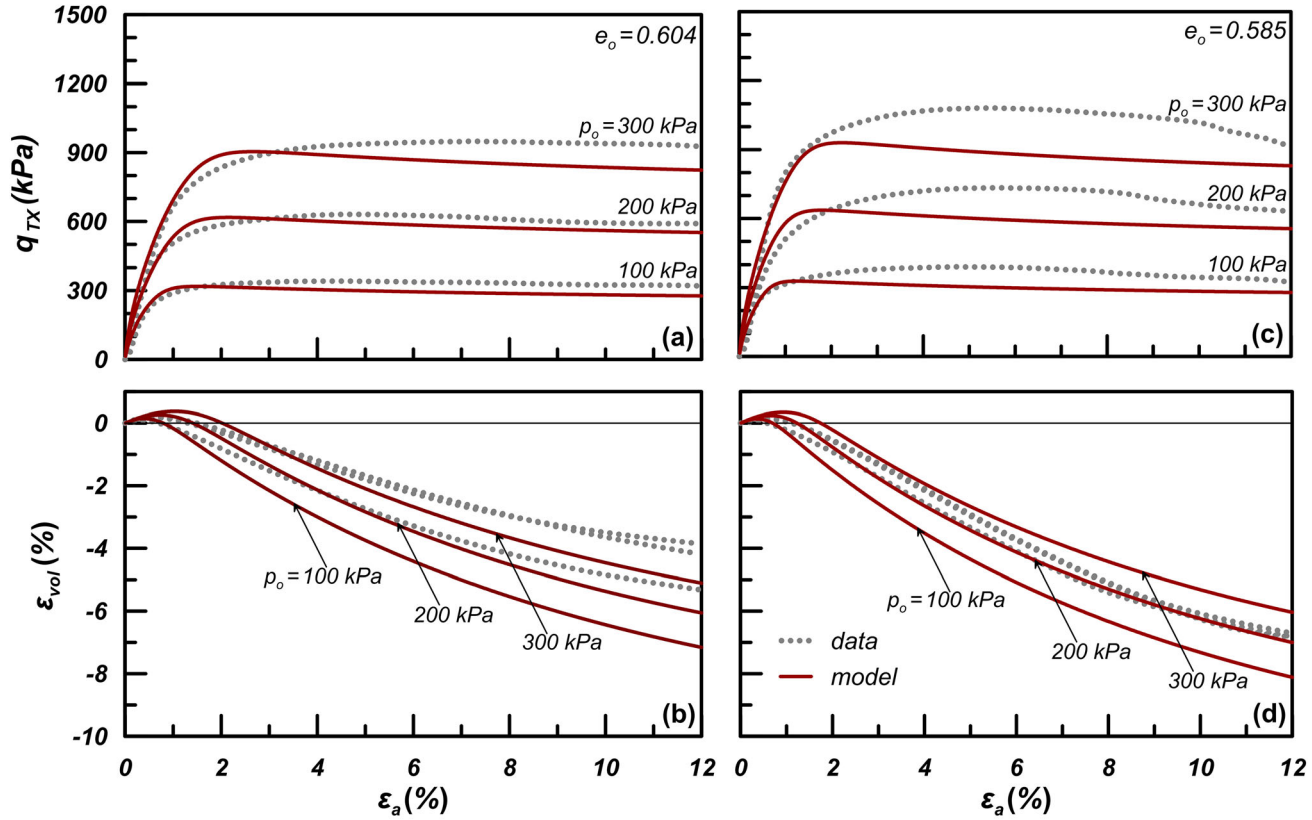

Fig. 9 Experimental results and model predictions of drained monotonic triaxial compression tests. Data on Ottawa-F65 sand after Vasko [63] and Vasko et al. [64]

performed by Yoshimine et al. [75], on isotropically consolidated samples of Toyoura sand. The initial mean effective stress p_o has a common value of 100 kPa for all samples, and the examined relative densities cover a range between loose and medium–dense conditions (e = 0.804–0.888, with $D_r \approx$ 22–45%). In all cases, the comparison is made in terms of effective stress paths $q = \sigma_1 - \sigma_3$ versus p (subplot a) and stress–strain relations

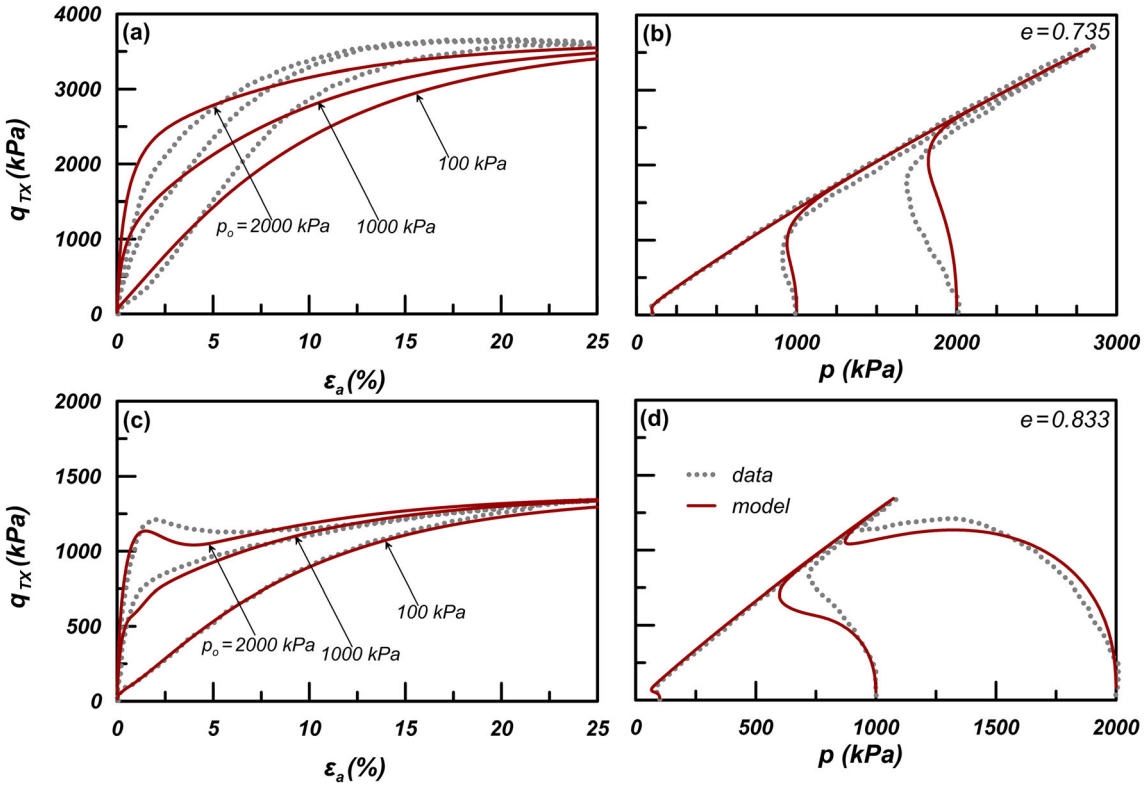

Fig. 10 Experimental results and model predictions of undrained monotonic triaxial compression tests. Data on Toyoura sand after Verdugo and Ishihara [65]

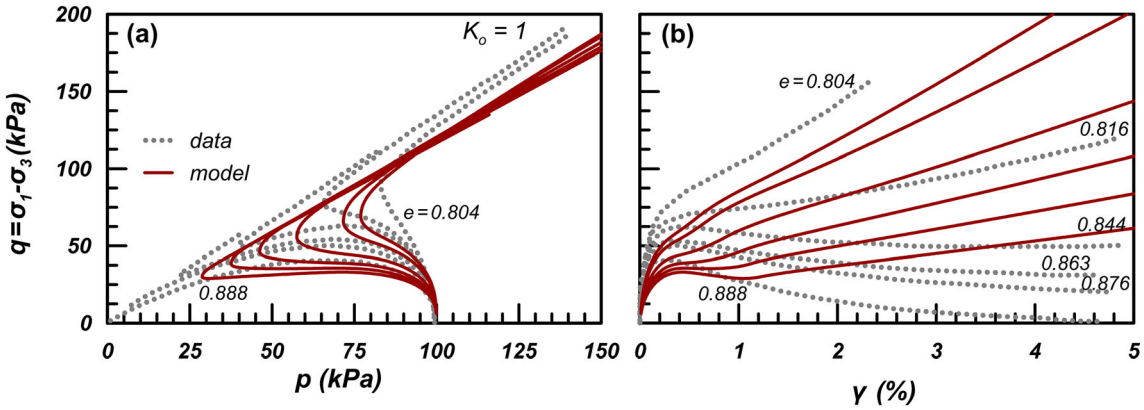

Fig. 11 Experimental results and model predictions of undrained monotonic simple shear tests (K_o = 1). Data on Toyoura sand after Yoshimine et al. [75]

q vs γ (subplot b). The simulations are fair for the most dilative of the examined densities and show a gradually increasing contractive response as the void ratio e increases. However, an under-prediction of the effect of void ratio e may be observed. This should not be considered as a shortcoming of the model, since it has been calibrated to provide satisfactory accuracy for a huge range of void ratio values of Toyoura sand, from e = 0.674 ($D_r \approx 81\%$ in Fig. 8) to e = 0.996 ($D_r < 0\%$ in Fig. 7).

4.2 Undrained cyclic loading

With the same set of parameters (listed in Table 2), undrained cyclic loading tests are simulated in this paragraph. Figure 12 shows the model capability in simulating

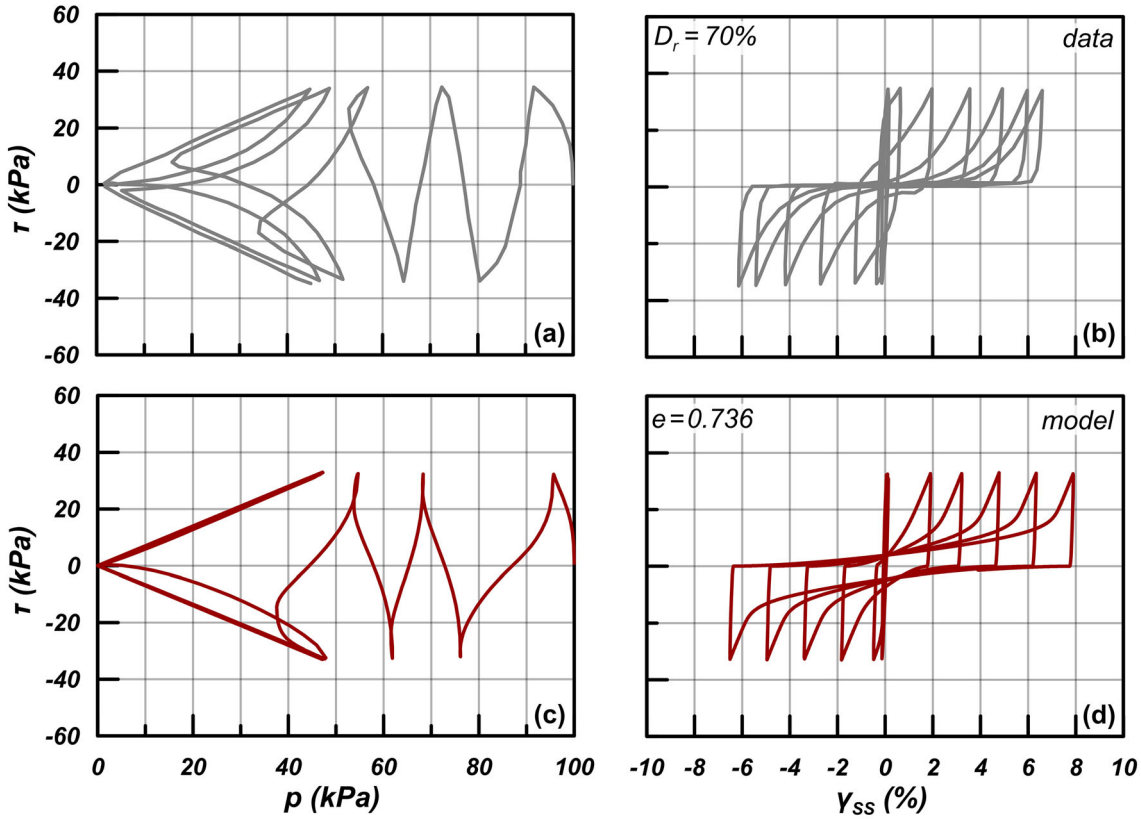

Fig. 12 Experimental results and model predictions of undrained cyclic torsional shear test. Data on Toyoura sand after Zhang [78]

an undrained cyclic torsional shear test conducted by Zhang [78] on Toyoura sand and presented by Zhang and Wang [77]. It was isotropically consolidated at p_o = 100 kPa and a relative density D_r = 70%, which according to the given values of e_{max} = 0.973 and e_{min} = 0.635 corresponds to a void ratio e equal to 0.736. The single amplitude of the cyclically applied shear stress for this test is τ_{cyc} = 33 kPa. The comparison is made in the spaces of shear stress τ versus mean effective stress p (subplots a, c) and τ vs shear strain γ_{SS} (subplots b, d). The comparison is quite satisfactory as the model successfully captures the cyclic mobility between loading–unloading paths and illustrates "*banana-shaped*" stress–strain (τ versus γ_{SS}) loops when approaching p = 0 (initial liquefaction). Moreover, shear strain continuously increases during the cyclic shearing after liquefaction triggering in good agreement with the experimental data.

Then, in Fig. 13, the model is evaluated against an undrained cyclic triaxial test on Ottawa-F65 sand, performed by El Ghoraiby et al. [19]. The test is performed for e = 0.585, and the sample was initially consolidated at a mean effective stress of 100 kPa. The comparison is made in the spaces of q_{TX} versus radial effective stress σ_r (effective stress path in subplots a, c) and q_{TX} vs axial strain ε_a (stress–strain relation in subplots b, d). The test is performed as stress controlled with a single amplitude of cyclic stress $q_{TX,cyc}$ = 34 kPa. Both the effective stress path and the stress–strain relation are captured quite well by the model. Observe how the model predicts well the initially decreasing rate of excess pore-pressure build-up with cycles and then how this rate increases to bring the sand to initial liquefaction. This non-constant rate of excess pore-pressure build-up is typical of sand response; however, it is rarely commented on in the literature of constitutive models for liquefaction, despite its importance for accurate simulations of boundary value problems. On the other hand, the model shows small bias in strain accumulation in the stress–strain relation (q_{TX} versus ε_a) toward the extension side. This is attributed to the different shear strengths in triaxial compression and extension, which lead to different strain accumulation rates. This bias is a common shortcoming of constitutive models aiming at liquefaction response (e.g., [17]) and has been hereby reduced, yet not alleviated, due to the introduction of the post-liquefaction constitutive ingredient $h_{post\text{-}liq}$ of Eq. (41). Note also here that this bias is not evidenced in cyclic loading in simple shear or torsional shear (e.g., in Fig. 12) where the Lode angle θ change within a loading cycle is very small in comparison with the "*jump*" between θ = 0° and θ = 60° in cyclic triaxial loadings. This is why any model aiming at

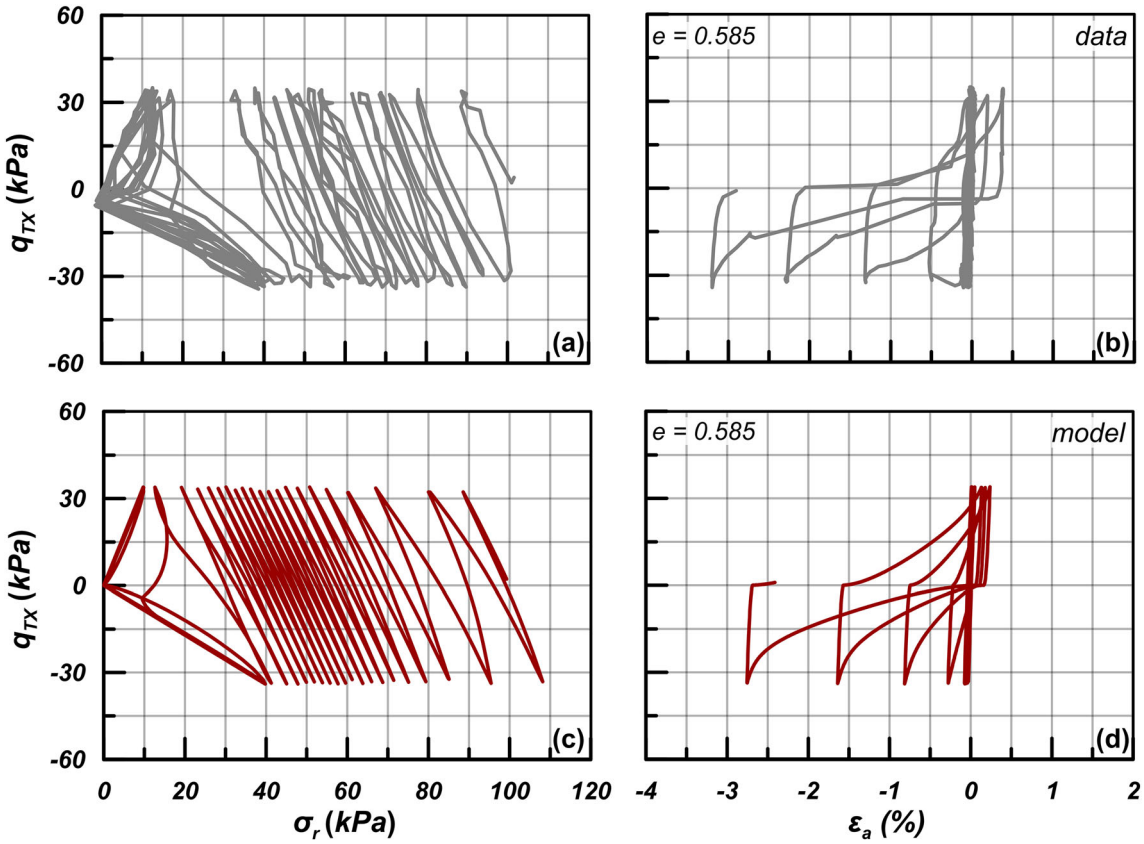

Fig. 13 Experimental results and model predictions of undrained cyclic triaxial test. Data on Ottawa-F65 sand after El Ghoraiby et al. [19]

successful liquefaction predictions should always be verified in both triaxial and simple shear or torsional cyclic loading.

4.2.1 Liquefaction resistance curves for different relative densities

Liquefaction resistance curves are a practical tool for assessing the simulation success for undrained cyclic loading, since they provide a grouping of many element tests for different cyclic stress ratio amplitudes, relative densities and stress levels and even different loading conditions. Toyoura sand is one of the most widely used sands for the study of liquefaction, so there is a plethora of experimental liquefaction resistance curves published by different researchers worldwide. Given the use of different Toyoura sand batches, there is significant scatter in the pertinent data, even when referring to the same values of relative density, initial stress level, as well as the same preparation method or loading type. Hence, it was deemed fairer to evaluate the model's accuracy in predicting liquefaction resistance through comparison with a group of liquefaction resistance curves of Toyoura sand from the literature ([23, 32, 60, 69, 73]) instead of a single set of curves.

In this perspective, in Fig. 14 a wide range of liquefaction resistance curves from cyclic triaxial tests is presented. The grouping of the experimental data was based on the relative density D_r of the sand, in groups of test data with D_r = 45% (subplot a), 60% (subplot b) and 75-80% (subplot c). Notice that there is a large deviation between the referenced values of e_{min} (0.597–0.635) and e_{max} (0.970–0.990) in the employed studies. Hence, since the model requires values of void ratio e and not D_r, their calculation is based on the average values of e_{min} = 0.609 and e_{max} = 0.976 that were estimated on the basis of the employed studies. So, the simulated void ratio for D_r = 45% is 0.811, for D_r = 60% is 0.756 and for D_r = 77.5% (a mean value between 75 and 80%) is 0.691. To reduce the scatter of the experimental results, all selected literature liquefaction resistance curves refer to isotropically consolidated samples at initial mean effective stress p_o = 100 kPa which are prepared with the method of air pluviation, except for the data of Yamashita and Toki [73] at D_r = 80%, where the vibration method was used. The comparison is made in terms of cyclic stress ratio *CSR* (= $q_{TX,cyc}$ /2p_o) versus N_l, the number of cycles required

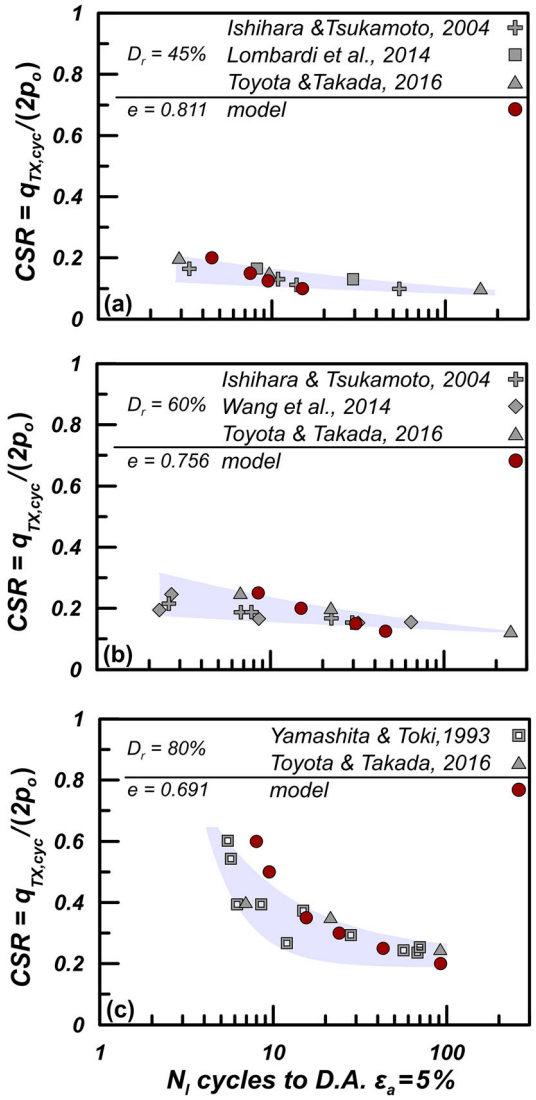

Fig. 14 Experimental results and model predictions of liquefaction resistance curves on the basis of undrained cyclic triaxial tests. Data on Toyoura sand after [23, 32, 60, 69, 73]

for a double amplitude axial strain equal to 5% to be developed. Observe that the liquefaction resistance curves procuring from the simulations generally plot within the range of the experimental data, albeit showing a slightly steeper inclination. However, it should be acknowledged that the typical experimental observation of no-liquefaction ($N_l \rightarrow \infty$) at small *CSR* values is well captured by the model, i.e., the model remedies a common shortcoming of liquefaction models (e.g., [1]). Moreover, the model simulates well the experimentally established increase in liquefaction resistance with relative density.

Subsequently, Fig. 15 presents the liquefaction resistance curves for the undrained cyclic triaxial tests on Ottawa-F65 conducted by El Ghoraiby et al. [19]. The comparison is made for two void ratios, e = 0.585 and

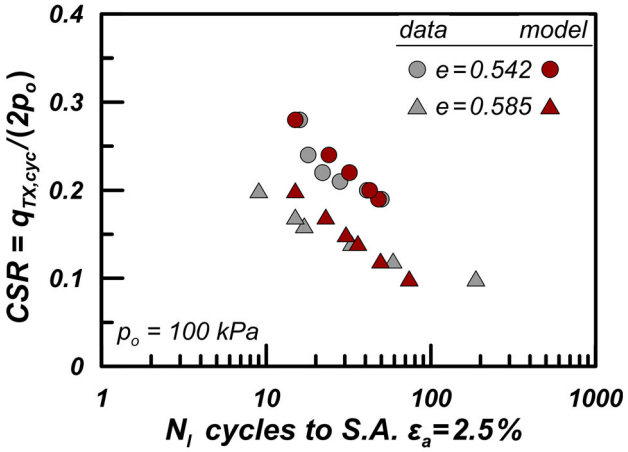

Fig. 15 Experimental results and model predictions of liquefaction resistance curves on the basis of undrained cyclic triaxial tests. Data on Ottawa-F65 sand after El Ghoraiby et al. [19]

e = 0.542, corresponding to $D_r \approx 60$ and 80% according to the values of e_{min} = 0.492 and e_{max} = 0.739 reported by Vasko [63]. The experimental data and the simulations are compared in terms of *CSR* vs cycles N_l to reach axial strain of single amplitude equal to 2.5%. The simulations are in good agreement with the model predictions, with a slightly steeper inclination for the case of e = 0.585 predicted by the model. Notice again the ability of the model to accurately predict the effect of relative density on liquefaction resistance, as well as the prediction of no-liquefaction when a small *CSR* ratio is applied.

4.2.2 Effect of confining stress level on liquefaction resistance

As already discussed above, the effect of overburden stress on cyclic resistance ratio *CRR* is often expressed and quantified in terms of a correction factor, known as K_σ, which is defined as:

$$K_\sigma = \frac{CRR_{\sigma_{a,o}}}{CRR_{\sigma_{a,o=100kPa}}} \tag{49}$$

In order to assess the ability of the model in predicting the K_σ factor, the undrained cyclic triaxial test simulations for Toyoura sand that are presented in Fig. 14 and referred to $p_o = \sigma_{a,o}$ = 100 kPa are now repeated for higher levels of initial mean effective stress, namely p_o = 200 kPa and 400 kPa, without changing the void ratio values. By comparing the *CRR* values obtained at 15 uniform loading cycles (in compliance with other studies, e.g., [8]), the values of K_σ are thus predicted for different $\sigma_{a,o}$ and D_r values. The same procedure is then followed for estimating K_σ values for undrained cyclic simple shear tests of Toyoura sand, for the same initial states ($\sigma_{a,o}$ and e). These

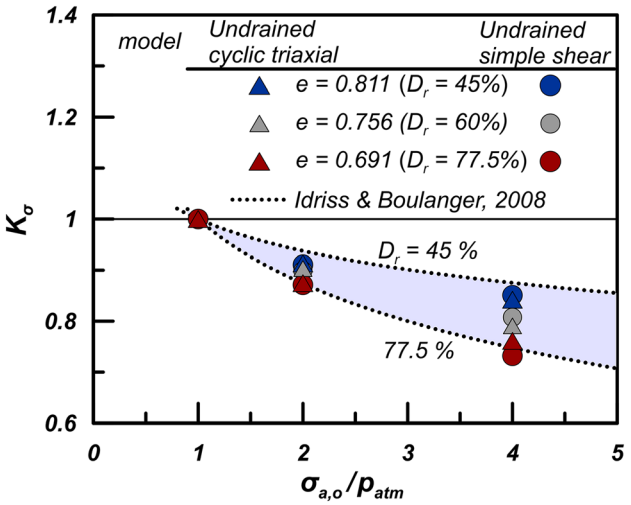

Fig. 16 Comparison of K_σ values for different loading type and different relative density D_r values predicted by the model for Toyoura sand versus the empirical relation of Idriss and Boulanger [22]

values are compared to the well-established empirical curves of Idriss and Boulanger [22] in Fig. 16. The comparison shows very good agreement with the literature, i.e., the model predicts accurately that liquefaction resistance decreases with increasing confining stresses and that the rate of decrease is nonlinear. Moreover, the model also predicts that the cyclic strengths for dense sands are comparatively more affected by confining stress than what is observed for loose sands.

4.3 Drained cyclic loading

4.3.1 Shear modulus degradation and damping ratio increase with cyclic strain

Figure 17 shows the normalized secant shear modulus G/G_{max} degradation curves (subplot a) and the damping ratio ξ increase curves (subplot b) derived from simulations of strain-controlled cyclic simple shear loading of both sands of interest. The horizontal axis of both diagrams depicts the single amplitude cyclic shear strain $\gamma_{SS,cyc}$ of the performed numerical simulations. The secant shear modulus G and the corresponding damping ratio ξ refer to the 1st cycle of loading, while the initial void ratio e_o is selected to correspond to an initial $D_r \approx 60\%$ for both examined sands ($e = 0.756$ for Toyoura, $e = 0.585$ for Ottawa-F65). Two extreme values of initial effective axial stress $\sigma_{a,o}$ are examined, namely 100kPa and 1000 kPa. In terms of shear modulus degradation, the results predicted by the model are consistent with the empirical relation proposed by Darendeli [15] for both examined sands, while they exhibit a less pronounced nonlinearity with respect to the Vucetic and Dobry [67] curve. Moreover, the simulated G/G_{max} reduction shows a dependency on stress level consistent with the empirical relations. In terms of damping ratio ξ, the results of the new model up to the strain level of 0.1%-especially for the Ottawa-F65 sand - are compared satisfactorily with the empirical relations. However, for larger strain levels, there is an over-prediction of ξ values, especially at the lower stress level. As explained by Taborda et al. [55], this is a well-known problem of constitutive models that comply with original Masing rules ([36]), and this model is no exception. At least, significant over-prediction appears only for very large cyclic shear

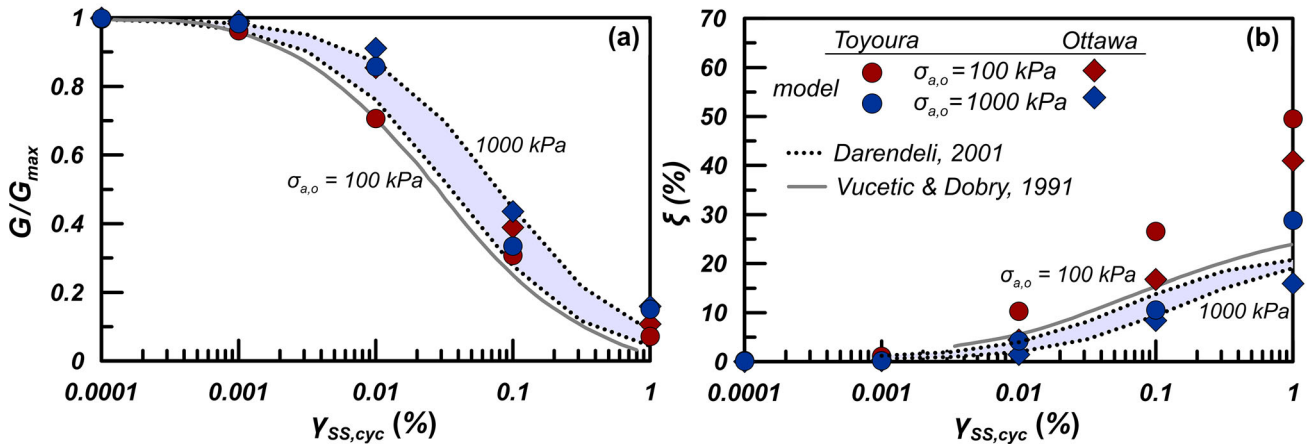

Fig. 17 Comparison of **a** shear modulus degradation curves and **b** damping ratio increase curves predicted by the model for both Toyoura and Ottawa-F65 sands versus the empirical relations of Darendeli [15] and Vucetic and Dobry [67]

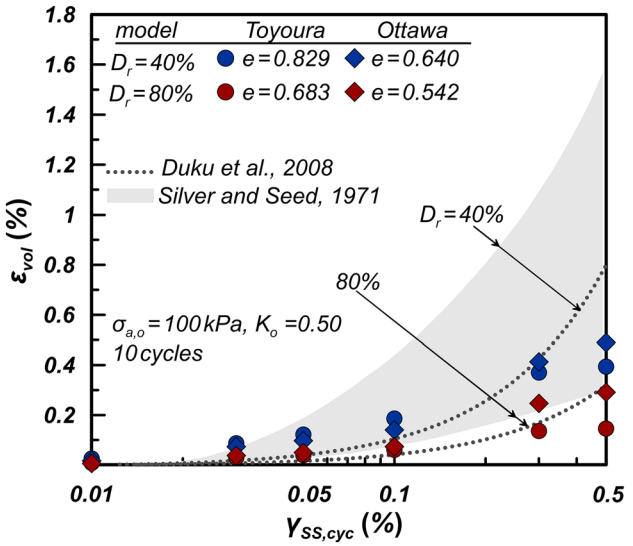

Fig. 18 Comparison of accumulated volumetric strains from drained cyclic simple shear tests predicted by the model for both Toyoura and Ottawa-F65 sands versus the empirical relations of Duku et al. [16] and the range of experimental data of Silver and Seed [53]

strains (e.g., $\gamma_{SS,cyc}$ = 1%) that are not very common in boundary value problems of practice, and only for low vertical stresses (e.g., in free-field conditions). It should be underlined here that evaluating model accuracy in terms of G/G_{max} versus $\gamma_{SS,cyc}$ curves makes sense, only if the G_{max} value is accurately predicted. In the proposed model, the G_{max} is calibrated directly on the basis of very small-strain measurements (e.g., see Fig. 5 for Toyoura sand) and thus satisfies this requirement.

4.3.2 Accumulation of strains with cycles

Figure 18 presents a summary of predicted values of accumulated volumetric strains ε_{vol} after 10 cycles of strain-controlled drained simple shear loading, at various levels of single amplitude cyclic shear strains $\gamma_{SS,cyc}$ ranging from 0.01% to 0.5%, for Toyoura and Ottawa-F65 sand. The initial relative densities of 40% and 80%, which correspond to initial void ratios of e_o = 0.829 and e_o = 0.683 for Toyoura sand and e_o = 0.640 and e_o = 0.542 for Ottawa-F65 sand, are examined. The samples are consolidated at an initial effective axial stress $\sigma_{a,o}$ = 100 kPa, and a K_o value equal to 0.50 is applied. The predicted values are compared with the empirical relations of Duku et al. [16], considering the proposed values of the parameters by the authors, as well as the range of experimental data of Silver and Seed [53]. It is observed that, on the whole, the comparison is acceptable. Specifically, at small and intermediate $\gamma_{SS,cyc}$ strain levels, the predicted volumetric strains by the model are closer to the range of experimental data of Silver and Seed [53], while at larger

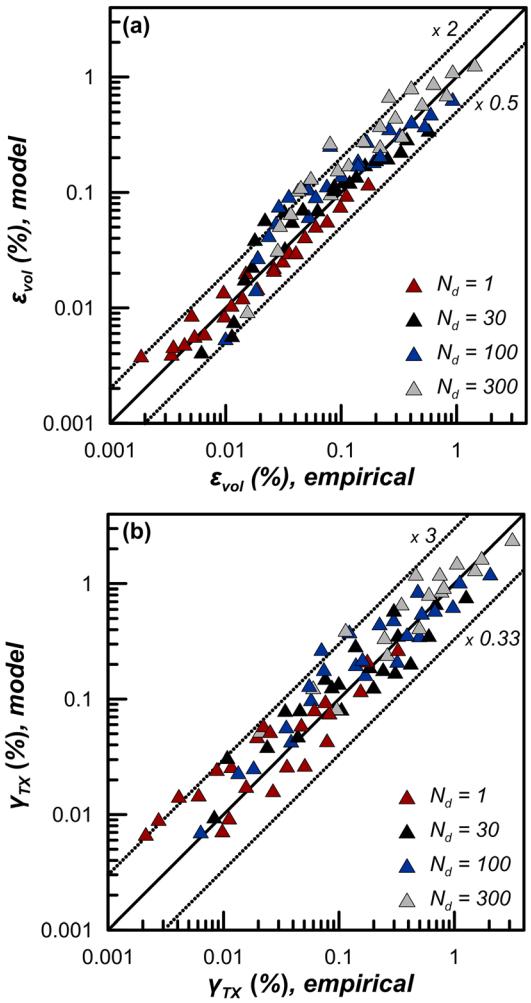

Fig. 19 Comparison of accumulated **a** volumetric strains and **b** shear strains from drained cyclic triaxial tests predicted for Toyoura sand by the model and by the empirical relations of Bouckovalas et al. [7] and Stamatopoulos et al. [54]

$\gamma_{SS,cyc}$ strain levels, the accumulation of volumetric strains is more in accordance with the empirical relations of Duku et al. [16]. Moreover, the qualitative dependency of accumulated volumetric strains on relative density D_r is reasonably consistent with the empirical data. Finally, note that the form given to the dilatancy function in contraction, as well as the inclusion of the enhanced formulation for addressing the overshooting problem, reduce significantly strain accumulation at very small $\gamma_{SS,cyc}$ strains. As such, the ε_{vol} accumulated in cyclic shearing with $\gamma_{SS,cyc}$ lower than a volumetric strain threshold γ_{tv} (e.g., smaller than 0.01% on average for sands) is insignificant.

Figure 19 presents a summary comparison of accumulated volumetric strains ε_{vol} (subplot a) and accumulated shear strains $\gamma_{TX} = \varepsilon_a - \varepsilon_r$ (subplot b) in cyclic drained triaxial tests as predicted by the new model versus the pertinent values from the empirical relations of Bouckovalas

et al. [7] and Stamatopoulos et al. [54]. Strain accumulation is measured after N_d = 1, 30, 100 and 300 cycles, which means that the model is hereby verified for boundary value problems that include many more cycles than what earthquakes produce. Specifically, only simulations using the calibration of Toyoura sand are performed here and the initial relative densities of D_r = 40%, 60% and 80%, with initial void ratios e_o = 0.829, 0.756 and 0.683 are examined. All simulated tests were anisotropically consolidated at a mean effective stress p_o = 200 kPa, with an appropriate combination of initial axial and radial stresses, so as initial stress ratios $q_{TX,o}/p_o$ = 0.35 (K_o = 0.716) and 0.75 (K_o = 0.50) to be attained after consolidation. The anisotropic consolidation permits, in addition to accumulation of ε_{vol} with cycles, to also study the concurrent accumulation of shear strains γ_{TX}. Hence, in both subplots of Fig. 19 different colors of symbols depict the different number of cycles, while the solid diagonal line is the locus of points of perfect agreement between predictions by the model and predictions by the empirical relations. Similarly, the two dashed lines define the loci of overestimation and underestimation by the denoted factor. In terms of accumulated volumetric strains ε_{vol} (subplot a), a quite good overall agreement is observed, as the ratio of predicted over empirical values ranges between 0.5 and 2. On the other hand, in terms of accumulated shear strains γ_{TX}, the comparison is less impressive, but remains satisfactory.

5 Conclusions and discussion

This paper presents a bounding surface plasticity model with reversal surfaces aiming to provide accurate simulations of both the monotonic response (until the critical state) and the cyclic response (for any shear strain level) of granular soils, irrespective of initial density and mean effective stress level, with a single set of model parameters. The paper presents the model formulation and the calibration process of its 14 parameters, firstly of the 12 parameters required for monotonic loading and then of the 2 additional parameters related to cyclic loading. Being a SANISAND-type model, the calibration process includes trial-and-error runs, for 5 of the 14 parameters. Model performance is verified against a large database of monotonic and cyclic shearing tests, both drained and undrained, on samples of Toyoura and Ottawa-F65 sand, covering a wide range of initial conditions in terms of mean effective stress p_o = 61 kPa to 2000 kPa, void ratio e_o = 0.542 to 0.996 and state parameter ψ_o = –0.253 to 0.084. Wherever sand-specific data are lacking, empirical relations are used for validating specific aspects of the response.

It should be clarified here that being of the SANISAND-type, the proposed model is accurate in monotonic or cyclic shearing paths where non-zero deviatoric stress ratio rates ($\dot{\boldsymbol{r}} \neq 0$) prevail, but underpredicts plastic strain in problems where loading under constant stress ratio appears (e.g., one-dimensional consolidation; see also [17]). Accounting for plastic strains due to such types of loading may require additional mechanisms for plastic strain rate development (e.g., [56] or [68]), but such complications are beyond the scope of this model. Similarly, this model is unable to capture the plastic strains appearing during effective stress principal axes rotation, due to the ensuing non-coaxiality between the stress and the plastic strain rate tensors. For SANISAND-type models additional plastic load mechanisms, or multiple dilatancy and plastic modulus expressions, or, in the simplest way, a reformulation of the dilatancy and plastic modulus expressions (e.g., [46, 72]) have been proposed to remedy this shortcoming. Again, such complexities are beyond the target of this model. Despite the foregoing limitations, the thorough verification process proves that the proposed is a useful general-purpose constitutive model for sands, since it provides the user with a satisfactory performance without a need for recalibration regardless of whether the boundary value problem is static, cyclic or dynamic in nature.

In closing, note that the proposed model (that can be briefly referred to hereafter as the LiPa model on the basis of the authors' surnames) has already been implemented in an explicit finite difference code with a u-p formulation. It has also been successfully verified against measurements from multiple dynamic centrifuge tests involving liquefaction of the same sand, all with a single set of values for the model parameters. This validation process is complementary to the one presented herein and satisfies the notion of Manzari and El Ghoraiby [35] who consider such a validation preferable to mere comparison with element test data, but is beyond the scope of this paper that emphasizes the constitutive formulation. It may be found in Limnaiou and Papadimitriou [29].

Appendix

This section presents Table 3 and Table 4 that summarize the information about the laboratory tests employed in the model validation process, i.e., in Figs. 7 through 19. This information includes the sand name, the type of test and its initial conditions in terms of void ratio e_o, axial effective stress $\sigma_{a,o}$, mean effective stress p_o and state parameter ψ_o.

See Tables 3 and 4.

Table 3 Initial conditions of tests used in model validation process against experimental data

Figure	Sand	Test*	Initial void ratio, e_o	Initial axial effective stress, $\sigma_{a,o}$	Initial mean effective stress, p_o	Initial state parameter, ψ_o
7	Toyoura	DM/TC	0.831	100	100 (K_o = 1)	−0.084
7	Toyoura	DM/TC	0.917	100	100 (K_o = 1)	0.002
7	Toyoura	DM/TC	0.996	100	100 (K_o = 1)	0.081
7	Toyoura	DM/TC	0.810	500	500 (K_o = 1)	−0.066
7	Toyoura	DM/TC	0.886	500	500 (K_o = 1)	0.010
7	Toyoura	DM/TC	0.960	500	500 (K_o = 1)	0.084
8	Toyoura	DM/TS	0.674	200	113.33 (K_o = 0.350**)	−0.239
8	Toyoura	DM/TS	0.798	100	61 (K_o = 0.415**)	−0.123
8	Toyoura	DM/TS	0.797	200	121.87 (K_o = 0.414**)	−0.115
9	Ottawa-F65	DM/TC	0.585	100	100 (K_o = 1)	−0.205
9	Ottawa-F65	DM/TC	0.585	200	200 (K_o = 1)	−0.192
9	Ottawa-F65	DM/TC	0.585	300	300 (K_o = 1)	−0.180
9	Ottawa-F65	DM/TC	0.604	100	100 (K_o = 1)	−0.186
9	Ottawa-F65	DM/TC	0.604	200	200 (K_o = 1)	−0.173
9	Ottawa-F65	DM/TC	0.604	300	300 (K_o = 1)	−0.161
10	Toyoura	UM/TC	0.735	100	100 (K_o = 1)	−0.180
10	Toyoura	UM/TC	0.735	1000	1000 (K_o = 1)	−0.105
10	Toyoura	UM/TC	0.735	2000	2000 (K_o = 1)	−0.046
10	Toyoura	UM/TC	0.833	100	100 (K_o = 1)	−0.082
10	Toyoura	UM/TC	0.833	1000	1000 (K_o = 1)	−0.007
10	Toyoura	UM/TC	0.833	2000	2000 (K_o = 1)	0.052
11	Toyoura	UM/SS	0.804	100	100 (K_o = 1)	−0.111
11	Toyoura	UM/SS	0.816	100	100 (K_o = 1)	−0.099
11	Toyoura	UM/SS	0.844	100	100 (K_o = 1)	−0.071
11	Toyoura	UM/SS	0.863	100	100 (K_o = 1)	−0.052
11	Toyoura	UM/SS	0.876	100	100 (K_o = 1)	−0.039
11	Toyoura	UM/SS	0.888	100	100 (K_o = 1)	−0.027
12	Toyoura	UCyc/TS	0.736	100	100 (K_o = 1)	−0.179
13	Ottawa-F65	UCyc/TX	0.585	100	100 (K_o = 1)	−0.205
14	Toyoura	UCyc/TX	0.811	100	100 (K_o = 1)	−0.104
14	Toyoura	UCyc/TX	0.756	100	100 (K_o = 1)	−0.159
14	Toyoura	UCyc/TX	0.691	100	100 (K_o = 1)	−0.224
15	Ottawa-F65	UCyc/TX	0.585	100	100 (K_o = 1)	−0.205
15	Ottawa-F65	UCyc/TX	0.542	100	100 (K_o = 1)	−0.248

*DM: Drained monotonic, UM: Undrained monotonic, DCyc: Drained cyclic, UCyc: Undrained cyclic

TC: Triaxial compression, TX: Triaxial, TS: Torsional shear, SS: Simple shear

** $K_o = 0.52e_o$ according to Pradhan et al. [47]

Table 4 Initial conditions of tests used in model validation process against empirical relations.

Figure	Sand	Test*	Initial void ratio, e_o	Initial axial effective stress, $\sigma_{a,o}$	Initial mean effective stress, p_o	Initial state parameter, ψ_o
16	Toyoura	UCyc/TX	0.811	100	100 (K_o = 1)	−0.104
16	Toyoura	UCyc/TX	0.811	200	200 (K_o = 1)	−0.092
16	Toyoura	UCyc/TX	0.811	400	400 (K_o = 1)	−0.073
16	Toyoura	UCyc/TX	0.756	100	100 (K_o = 1)	−0.159
16	Toyoura	UCyc/TX	0.756	200	200 (K_o = 1)	−0.147
16	Toyoura	UCyc/TX	0.756	400	400 (K_o = 1)	−0.128
16	Toyoura	UCyc/TX	0.691	100	100 (K_o = 1)	−0.224
16	Toyoura	UCyc/TX	0.691	200	200 (K_o = 1)	−0.212
16	Toyoura	UCyc/TX	0.691	400	400 (K_o = 1)	−0.193
16	Toyoura	UCyc/SS	0.811	100	100 (K_o = 1)	−0.104
16	Toyoura	UCyc/SS	0.811	200	200 (K_o = 1)	−0.092
16	Toyoura	UCyc/SS	0.811	400	400 (K_o = 1)	−0.073
16	Toyoura	UCyc/SS	0.756	100	100 (K_o = 1)	−0.159
16	Toyoura	UCyc/SS	0.756	200	200 (K_o = 1)	−0.147
16	Toyoura	UCyc/SS	0.756	400	400 (K_o = 1)	−0.128
16	Toyoura	UCyc/SS	0.691	100	100 (K_o = 1)	−0.224
16	Toyoura	UCyc/SS	0.691	200	200 (K_o = 1)	−0.212
16	Toyoura	UCyc/SS	0.691	400	400 (K_o = 1)	−0.193
17	Toyoura	DCyc/SS	0.756	100	100 (K_o = 1)	−0.159
17	Toyoura	DCyc/SS	0.756	1000	1000 (K_o = 1)	−0.084
17	Ottawa-F65	DCyc/SS	0.585	100	100 (K_o = 1)	−0.205
17	Ottawa-F65	DCyc/SS	0.585	1000	1000 (K_o = 1)	−0.114
18	Toyoura	DCyc/SS	0.829	100	66.67 (K_o = 0.50)	−0.091
18	Toyoura	DCyc/SS	0.683	100	66.67 (K_o = 0.50)	−0.237
18	Ottawa-F65	DCyc/SS	0.640	100	66.67 (K_o = 0.50)	−0.155
18	Ottawa-F65	DCyc/SS	0.542	100	66.67 (K_o = 0.50)	−0.253
19	Toyoura	DCyc/TX	0.829	246.67	200 ($q_{TX,o}/p_o$ = 0.35)	−0.074
19	Toyoura	DCyc/TX	0.756	246.67	200 ($q_{TX,o}/p_o$ = 0.35)	−0.147
19	Toyoura	DCyc/TX	0.683	246.67	200 ($q_{TX,o}/p_o$ = 0.35)	−0.220
19	Toyoura	DCyc/TX	0.829	300	200 ($q_{TX,o}/p_o$ = 0.75)	−0.074
19	Toyoura	DCyc/TX	0.756	300	200 ($q_{TX,o}/p_o$ = 0.75)	−0.147
19	Toyoura	DCyc/TX	0.683	300	200 ($q_{TX,o}/p_o$ = 0.75)	−0.220

*DCyc: Drained cyclic; UCyc: Undrained cyclic; TX: Triaxial; SS: Simple shear

Acknowledgements This scientific paper was supported by the Onassis Foundation-Scholarship ID: G ZO 013-1/2018-2019, awarded to the first author. In addition, the help of Dr. Yannis K. Chaloulos is gratefully acknowledged, for introducing the first author to the use of dynamic link library and to the problem of stress–strain overshooting. Finally, the authors express their gratitude to the 3 anonymous reviewers for their help in upgrading the quality of the paper.

References

1. Andrianopoulos KI, Papadimitriou AG, Bouckovalas GD (2010) Bounding surface plasticity model for the seismic liquefaction analysis of geostructures. Soil Dyn Earthq Eng 30:895–911. https://doi.org/10.1016/j.soildyn.2010.04.001
2. Arulmoli K, Muraleetharan KK, Hossain MM, Fruth LS (1992) VELACS: Verification of liquefaction analysis by centrifuge studies, Laboratory testing program - Soil Data Report. The Earth Techn Corp, Irvine, CA
3. Barrero AR, Taiebat M, Dafalias YF (2020) Modeling cyclic shearing of sands in the semifluidized state. Int J Numer Anal Methods Geomech 44:371–388. https://doi.org/10.1002/nag.3007
4. Bastidas AMP (2016) Ottawa F-65 sand characterization. PhD Thesis. University of California, Davis.
5. Bauer, E., & Wu, W. (1993). A hypoplastic model for granular soils under cyclic loading. In Proceed. of the Int. Workshop on Modern Approaches to Plasticity, pp 247–258
6. Been K, Jefferies MG (1985) A state parameter for sands. Géotechnique 35:99–112. https://doi.org/10.1680/geot.1985.35.2.99
7. Bouckovalas G, Whitman RV, Marr WA (1984) Permanent displacement of sand with cyclic loading. J Geotech Eng

110:1606–1623. https://doi.org/10.1061/(ASCE)0733-9410(1984)110:11(1606)
8. Boulanger RW, Ziotopoulou K (2013) Formulation of a sand plasticity plane-strain model for earthquake engineering applications. Soil Dyn Earthq Eng 53:254–267. https://doi.org/10.1016/j.soildyn.2013.07.006
9. Chaloulos YK, Papadimitriou AG, Dafalias YF (2019) Fabric effects on strip footing loading of anisotropic sand. J Geotech Geoenviron Eng 145(10):04019068-1-04019068-15. https://doi.org/10.1061/(asce)gt.1943-5606.0002082
10. Cheng Z, Detournay C (2021) Formulation, validation and application of a practice-oriented two-surface plasticity sand model. Comput Geotech 132(2021). https://doi.org/10.1016/j.compgeo.2020.103984
11. Dafalias YF (1986) Bounding surface plasticity. i: mathematical foundation and hypoplasticity. J Eng Mech 112:966–987. https://doi.org/10.1061/(ASCE)0733-9399(1986)112:9(966)
12. Dafalias YF, Manzari MT (2004) Simple plasticity sand model accounting for fabric change effects. J Eng Mech 130:622–634. https://doi.org/10.1061/(ASCE)0733-9399(2004)130:6(622)
13. Dafalias YF, Popov EP (1975) A model of nonlinearly hardening materials for complex loading. Acta Mech 21:173–192. https://doi.org/10.1007/BF01181053
14. Dafalias YF, Taiebat M (2016) SANISAND-Z: zero elastic range sand plasticity model. Géotechnique 66:999–1013. https://doi.org/10.1680/jgeot.15.P.271
15. Darendeli M (2001) Development of a new family of normalized modulus reduction and material damping curves. PhD Thesis. The University of Texas at Austin
16. Duku PM, Stewart JP, Whang DH, Yee E (2008) Volumetric strains of clean sands subject to cyclic loads. J Geotech Geoenviron Eng 134:1073–1085. https://doi.org/10.1061/(ASCE)1090-0241(2008)134:8(1073)
17. Duque J, Yang M, Fuentes W, Masin D, Taiebat M (2021) Characteristic limitations of advanced plasticity and hypoplasticity models for cyclic loading of sands. Acta Geotech. https://doi.org/10.1007/s11440-021-01418-z
18. Van Eekelen HAM (1980) Isotropic yield surfaces in three dimensions for use in soil mechanics. Int J Numer Anal Methods Geomech 4:89–101. https://doi.org/10.1002/nag.1610040107
19. El Ghoraiby M, Park H, Manzari M (2018) PRJ-1783: LEAP-2017 GWU Laboratory Tests. DesignSafe-CI/NHERI, Dataset. https://doi.org/10.17603/DS2210X
20. Elgamal A, Yang Z, Parra E, Ragheb A (2003) Modeling of cyclic mobility in saturated cohesionless soils. Int J Plast 19:883–905. https://doi.org/10.1016/S0749-6419(02)00010-4
21. Hardin BO (1978) The nature of stress-strain behavior for soils. In Proceed. of the ASCE Spec. Conference on Earth Engrg and Soil Dyn, State-of-the-art Rep, ASCE, New York, pp 3–90
22. Idriss IM, Boulanger RW (2008) Soil liquefaction during earthquakes. Monograph MNO-12. Earthquake Engineering Research Institute, Oakland, CA
23. Ishihara K, Tsukamoto Y (2004) Cyclic strength of imperfectly saturated sands and analysis of liquefaction. Proc Japan Acad Ser B 80:372–391. https://doi.org/10.2183/pjab.80.372
24. Kammerer AM, Wu J, Pestana JM, Riemer M, Seed RB (2000) Cyclic simple shear testing of Nevada sand for PEER center project 2051999. Geotechnical Engineering Rep. No. UCBGT-2000-01. Univ. of California, Berkeley, CA
25. Kolymbas D (2012) Barodesy: a new hypoplastic approach. Int J Numer Anal Methods Geomech 36:1220–1240. https://doi.org/10.1002/nag.1051
26. Li XS, Dafalias YF (2000) Dilatancy for cohesionless soils. Geotechnique 50:449–460. https://doi.org/10.1680/geot.2000.50.4.449
27. Li Z, Liu H (2020) An isotropic-kinematic hardening model for cyclic shakedown and ratcheting of sand. Soil Dyn Earthq Eng 138:106329. https://doi.org/10.1016/j.soildyn.2020.106329
28. Li XS, Wang Y (1998) Linear representation of steady-state line for sand. J Geotech Geoenvironmental Eng 124:1215–1217. https://doi.org/10.1061/(ASCE)1090-0241(1998)124:12(1215)
29. Limnaiou TG, Papadimitriou AG Verification of bounding surface plasticity model with reversal surfaces for the analysis of liquefaction problems. Soil Dyn Earthq Eng (under review)
30. Liu HY, Abell JA, Diambra A, Pisanò F (2019) Modelling the cyclic ratcheting of sands through memory-enhanced bounding surface plasticity. Géotechnique 69:783–800. https://doi.org/10.1680/jgeot.17.P.307
31. Liu H, Diambra A, Abell JA, Pisanò F (2020) Memory-enhanced plasticity modeling of sand behavior under undrained cyclic loading. J Geotech Geoenviron Eng 146:04020122. https://doi.org/10.1061/(asce)gt.1943-5606.0002362
32. Lombardi D, Bhattacharya S, Hyodo M, Kaneko T (2014) Undrained behaviour of two silica sands and practical implications for modelling SSI in liquefiable soils. Soil Dyn Earthq Eng 66:293–304. https://doi.org/10.1016/j.soildyn.2014.07.010
33. Loukidis D, Salgado R (2009) Modeling sand response using two-surface plasticity. Comput Geotech 36:166–186. https://doi.org/10.1016/j.compgeo.2008.02.009
34. Manzari MT, Dafalias YF (1997) A critical state two-surface plasticity model for sands. Géotechnique 47:255–272. https://doi.org/10.1680/geot.1997.47.2.255
35. Manzari, M.T., ElGhoraiby, M.A. (2021). On Validation of a Two-Surface Plasticity Model for Soil Liquefaction Analysis. In: Barla, M., Di Donna, A., Sterpi, D. (eds) Challenges and Innovations in Geomechanics. IACMAG 2021. Lecture Notes in Civil Engineering, vol 125. Springer, Cham. https://doi.org/10.1007/978-3-030-64514-4_76
36. Masing G (1926) Eigenspannungen und verfestigung beim messing (Self stretching and hardening for brass) (in German). In Proceed. of 2nd International Congress of Applied Mechanics. Zurich, Switzerland, pp 332–335
37. McAllister G, Taiebat M, Ghofrani A, Chen L, Arduino P (2015) Nonlinear site response analyses and high frequency dilation pulses. In Proceed. of 68th Canadian Geotechnical Conference, Quebec, QC, Canada
38. Mroz Z, Zienkiewicz O (1984) Uniform formulation of constitutive equations for clays and sand. In: Desai C, Gallagher R (eds) Mechanics of engineering materials. Wiley, United States, pp 415–450
39. Mróz Z, Norris VA, Zienkiewicz OC (1979) Application of an anisotropic hardening model in the analysis of elasto–plastic deformation of soils. Géotechnique 29:1–34. https://doi.org/10.1680/geot.1979.29.1.1
40. Mulilis P, Arulanandan K, Mitchell JK et al (1977) Effects of sample preparation on sand liquefaction. J Geotech Eng Div 103:91–108
41. Niemunis A, Herle I (1997) Hypoplastic model for cohesionless soils with elastic strain range. Mech Cohesive-frictional Mater 2:279–299. https://doi.org/10.1002/(SICI)1099-1484(199710)2:4<279::AID-CFM29>3.0.CO;2-8
42. Papadimitriou AG, Bouckovalas GD (2002) Plasticity model for sand under small and large cyclic strains: a multiaxial formulation. Soil Dyn Earthq Eng 22:191–204. https://doi.org/10.1016/S0267-7261(02)00009-X
43. Papadimitriou AG, Bouckovalas GD, Dafalias YF (2001) Plasticity model for sand under small and large cyclic strains. J Geotech Geoenvironmental Eng 127:973–983. https://doi.org/10.1061/(ASCE)1090-0241(2001)127:11(973)
44. Papadimitriou AG, Chaloulos YK, Dafalias YF (2019) A fabric-based sand plasticity model with reversal surfaces within

anisotropic critical state theory. Acta Geotech 14:253–277. https://doi.org/10.1007/s11440-018-0751-5
45. Papadimitriou AG, Chaloulos YK, Dimoula MK, Dafalias YF (2021) Importance of sand fabric anisotropy on fault rupture-foundation interaction. In: Barla M, Di Donna A, Sterpi D (eds) Challenges and innovations in geomechanics. Springer, Cham, pp 731–738. https://doi.org/10.1007/978-3-030-64514-4_77
46. Petalas AL, Dafalias YF, Papadimitriou AG (2019) SANISAND-FN: an evolving fabric-based sand model accounting for stress principal axes rotation. Int J Numer Anal Methods Geomech 43:97–123. https://doi.org/10.1002/nag.2855
47. Pradhan TBS, Tatsuoka F, Horii N (1988) Strength and deformation characteristics of sand in torsional simple shear. Soils Found 28:131–148. https://doi.org/10.3208/sandf1972.28.3_131
48. Ramberg W, Osgood WR (1943) Description of stress-strain curve by three parameters. Technical Note 902, National Advisory Committee for Aeronautics, Washington, D.C.
49. Rowe PW (1962) The stress-dilatancy relation for static equilibrium of an assembly of particles in contact. Proc R Soc London Ser A Math Phys Sci 269:500–527. https://doi.org/10.1098/rspa.1962.0193
50. Schofield A, Wroth P (1968) Critical state soil mechanics. McGraw-Hill, USA
51. Shahnazari H, Towhata I (2002) Torsion shear tests on cyclic stress-dilatancy relationship of sand. Soils Found 42:105–119. https://doi.org/10.3208/sandf.42.105
52. Shibuya S, Park C-S, Tatsuoka F et al (1994) The significance of local lateral-strain measurement of soil specimens for a wide range of strain. Soils Found 34:95–105. https://doi.org/10.3208/sandf1972.34.2_95
53. Silver ML, Seed HB (1971) Volume changes in sands due to cyclic loading. J Soil Mech Found Div 97(9):1171–1182
54. Stamatopoulos CA, Bouckovalas G, Whitman RV (1991) Analytical prediction of earthquake-induced permanent deformations. J Geotech Eng 117:1471–1491. https://doi.org/10.1061/(ASCE)0733-9410(1991)117:10(1471)
55. Taborda DMG, Zdravković L, Kontoe S, Potts DM (2014) Computational study on the modification of a bounding surface plasticity model for sands. Comput Geotech 59:145–160. https://doi.org/10.1016/j.compgeo.2014.03.005
56. Taiebat M, Dafalias YF (2008) SANISAND: simple anisotropic sand plasticity model. Int J Numer Anal Methods Geomech 32:915–948. https://doi.org/10.1002/nag.651
57. Tasiopoulou P, Gerolymos N (2016) Constitutive modeling of sand: formulation of a new plasticity approach. Soil Dyn Earthq Eng 82:205–221. https://doi.org/10.1016/j.soildyn.2015.12.014
58. Tasiopoulou P, Ziotopoulou K, Humire F, Giannakou A, Chacko J, Travasarou T (2020) Development and implementation of semiempirical framework for modeling postliquefaction shear deformation accumulation in sands. J Geotech Geoenviron Eng 146:04019120. https://doi.org/10.1061/(asce)gt.1943-5606.0002179
59. Tatsuoka F, Teachavorasinskun S, Dong J, Kohata Y, Sato T (1994) Importance of measuring local strains in cyclic triaxial tests on granular materials. In: Ebelhar RJ, Drnevich VP, Kutter BL, editors. Dynamics geotechnical testing II. ASTM. pp 288–302.
60. Toyota H, Takada S (2017) Variation of liquefaction strength induced by monotonic and cyclic loading histories. J Geotech Geoenviron Eng 143:04016120. https://doi.org/10.1061/(asce)gt.1943-5606.0001634
61. Tsaparli V, Kontoe S, Taborda DMG, Potts DM (2020) A case study of liquefaction: demonstrating the application of an advanced model and understanding the pitfalls of the simplified procedure. Géotechnique 70:538–558. https://doi.org/10.1680/jgeot.18.P.263
62. Vaid YP, Sivathayalan S (1996) Static and cyclic liquefaction potential of Fraser Delta sand in simple shear and triaxial tests. Can Geotech J 33:281–289. https://doi.org/10.1139/t96-007
63. Vasko A (2015) An investigation into the behavior of Ottawa Sand through Monotonic and Cyclic Shear Tests. Masters Thesis. The George Washington University
64. Vasko A, El Ghoraiby M, Manzari M (2018) PRJ-1780: LEAP-GWU-2015 Laboratory Tests. DesignSafe-CI/NHERI, Dataset. https://doi.org/10.17603/DS2TH7Q
65. Verdugo R, Ishihara K (1996) The steady state of sandy soils. Soils Found 36:81–91. https://doi.org/10.3208/sandf.36.2_81
66. Vucetic M (1994) Cyclic threshold shear strains in soils. J Geotech Eng 120:2208–2228. https://doi.org/10.1061/(ASCE)0733-9410(1994)120:12(2208)
67. Vucetic M, Dobry R (1991) Effect of soil plasticity on cyclic response. J Geotech Eng 117:89–107. https://doi.org/10.1061/(ASCE)0733-9410(1991)117:1(89)
68. Wang Z, Dafalias YF, Shen C (1990) Bounding surface hypoplasticity model for sand. J Eng Mech 116:983–1001. https://doi.org/10.1061/(ASCE)0733-9399(1990)116:5(983)
69. Wang H, Koseki J, Sato T (2014) Resistance against liquefaction of unsaturated Toyoura sand and Inagi sand. Bulletin of ERS 47:3-14. Institute of Industrial Science, University of Tokyo
70. Wicaksono RI, Kuwano R (2009) Small strain shear stiffness of Toyoura sand obtained from various wave measurement techniques. Bulletin of ERS 42:107–120. Institute of Industrial Science, University of Tokyo
71. Wu J, Kammerer A, Riemer M, Seed RB, Pestana JM (2004) Laboratory study of liquefaction triggering criteria. In: 13th World Conference on Earthquake Engineering Vancouver, B .C., Canada. Vancouver, B.C., Canada, August 1–6
72. Xue L, Yu J, Pan J, Wang R, Zhang JM (2021) Three-dimensional anisotropic plasticity model for sand subjected to principal stress value change and axes rotation. Int J Numer Anal Methods Geomech 45:353–381. https://doi.org/10.1002/nag.3159
73. Yamashita S, Toki S (1993) Effects of fabric anisotropy of sand on cyclic undrained triaxial and torsional strengths. Soils Found 33:92–104. https://doi.org/10.3208/sandf1972.33.3_92
74. Yang M, Taiebat M, Dafalias YF (2020) SANISAND-MSf: a sand plasticity model with memory surface and semifluidised state. Géotechnique. https://doi.org/10.1680/jgeot.19.p.363
75. Yoshimine M, Ishihara K, Vargas W (1998) Effects of principal stress direction and intermediate principal stress on undrained shear behavior of sand. Soils Found 38:179–188. https://doi.org/10.3208/sandf.38.3_179
76. Zhang W, Lim K, Ghahari SF, Arduino P, Taciroglu E (2021) On the implementation and validation of a three-dimensional pressure-dependent bounding surface plasticity model for soil nonlinear wave propagation and soil-structure interaction analyses. Int J Numer Anal Methods Geomech 45:1091–1119. https://doi.org/10.1002/nag.3194
77. Zhang JM, Wang G (2012) Large post-liquefaction deformation of sand, part I: physical mechanism, constitutive description and numerical algorithm. Acta Geotech 7:69–113. https://doi.org/10.1007/s11440-011-0150-7
78. Zhang JM (1997) Cyclic critical stress state theory of sand with its application to geotechnical problems. PhD Thesis. Tokyo Institute of Technology

Publisher's Note Springer Nature remains neutral with regard to jurisdictional claims in published maps and institutional affiliations.